POLITECNICO DI TORINO

Master's Degree in Aerospace engineering

Master's Degree Thesis

Advanced numerical modelling of a Vertical Axis Wind Turbine through CFD

Supervisors

Prof. GIOVANNI BRACCO

Prof. ORONZO DELL'EDERA

Prof. LORENZO DUTTO

Candidate

MATTEO BENEDETTO

OTTOBRE 2024

Abstract

Vertical Axis Wind Turbines (VAWTs) are a type of wind turbine where the rotor shaft is positioned vertically, allowing them to capture wind from any direction without the need for orientation mechanisms. These turbines are particularly suited for urban environments and locations with variable wind conditions, offering advantages in terms of design simplicity and ease of maintenance compared to traditional Horizontal Axis Wind Turbines (HAWTs). To better understand the behavior and performance of this type of turbine, a robust simulation methodology must be developed.

This thesis focuses on the study and simulation of VAWTs, aiming to enhance the understanding of their aerodynamic behavior and performance. The work is divided into three main phases. In the first phase, a review of existing literature on VAWTs is conducted. Next, a detailed 2D simulation of the turbine is set up, with particular attention given to the verification and evaluation of key simulation parameters, including mesh refinement, turbulence models, and boundary conditions. Finally, the second phase involves the validation of the 2D simulation results through 3D modeling, using experimental data from a reference study. The comparison between the simulated and experimental results provides insights into the accuracy of the computational models and highlights the potential for optimizing VAWT design and performance. The findings contribute to a deeper understanding of the simulation process and its applicability in predicting real-world turbine behavior, offering a foundation for further advancements in renewable energy technologies.

Table of Contents

List of Tables

List of Figures

Chapter 1

Vertical Axis Wind Turbines

Vertical Axis Wind Turbines (VAWTs) represent one of the earliest yet less prominent technologies in the realm of wind energy conversion. The concept of using wind power for mechanical purposes dates back thousands of years. Early VAWT models can be traced to ancient Persia (modern-day Iran) between 500 and 900 AD, where vertical-axis windmills were employed for tasks such as grinding grain and pumping water. These early machines utilized vertically aligned wooden blades attached to a central rotating shaft, driving basic agricultural mechanisms.

During the Middle Ages, European technological developments shifted towards Horizontal Axis Wind Turbines (HAWTs), which eventually became the prevailing wind power technology. HAWTs exhibited greater efficiency in regions with consistent wind patterns and, with the advent of industrialization, they were widely adopted for electricity generation and industrial milling.

In the 20th century, VAWTs experienced renewed attention, largely due to the work of Georges Darrieus in the 1930s. Darrieus designed a unique vertical-axis rotor with curved blades resembling a helical shape. Despite challenges with stability and the need for an external starting mechanism, the Darrieus turbine marked a significant milestone in VAWT development because of its high aerodynamic efficiency, sometimes exceeding that of contemporary HAWTs.

The energy crises of the 1970s spurred further interest in renewable energy, including VAWTs. Several notable designs emerged during this period:

- **Sandia National Laboratories Darrieus Turbine (1970s-1980s)**: One of the most significant VAWT research efforts, Sandia's project aimed to enhance the performance of large-scale Darrieus turbines. Their research culminated in the development of a 34-meter Darrieus turbine, operational from 1982 to 1988. This turbine demonstrated the feasibility of large-scale VAWT systems, though problems such as blade fatigue and maintenance difficulties limited widespread adoption [1].

- **H-rotor Design**: Another important innovation during this era was the H-rotor, a variant of the Darrieus turbine that employed straight blades connected by horizontal supports, forming an "H" shape. This design was easier to manufacture and provided greater structural stability. A well-known example is the Finnish 500 kW VAWT installed in Kotka in 1991, which operated for several years before decommissioning [2].

- **Gorlov Helical Turbine (1990s)**: An evolution of the Darrieus turbine, the Gorlov turbine featured helical blades designed to mitigate torque pulsations, resulting in smoother operation. This design improved both efficiency and reliability, particularly in environments with variable wind conditions.

Despite these advances, VAWTs remained less prevalent than HAWTs throughout the late 20th and early 21st centuries. Nevertheless, VAWTs have several intrinsic advantages, including their ability to capture wind from any direction and their mechanical simplicity due to the absence of yaw mechanisms. These characteristics make VAWTs particularly suitable for urban settings and locations with turbulent wind conditions.

In recent years, progress in computational modeling and aerodynamic research has sparked renewed interest in VAWTs within both academia and industry. Using advanced simulation tools and modern lightweight, durable materials, new VAWT designs are being optimized for enhanced efficiency and performance. This thesis contributes to the field by investigating the aerodynamic behavior of VAWTs through numerical simulations and validating these findings with experimental data, aiming to improve the design and competitiveness of VAWTs in modern wind energy applications.
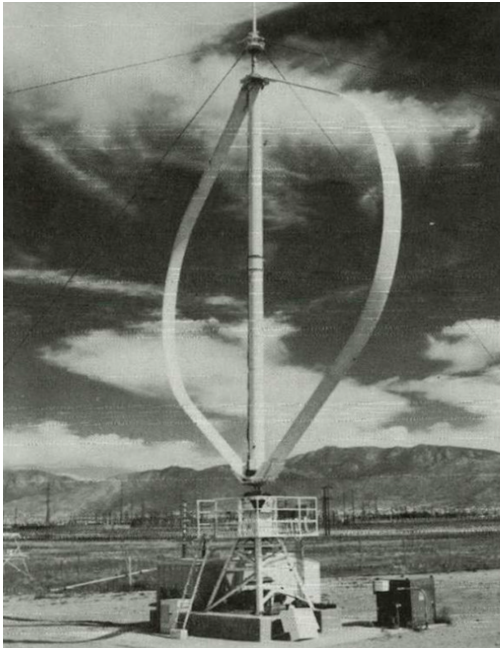
(a) The Sandia National Laboratories Darrieus turbine

(b) The Gorlov Helical turbine

Figure 1.1: Comparison of the Sandia Darrieus turbine and the Gorlov Helical turbine

1.1 Comparison between VAWT and HAWT

Vertical Axis Wind Turbines (VAWTs) and Horizontal Axis Wind Turbines (HAWTs) exhibit several key differences [3], which are summarized below:

- **Rotor Orientation:** VAWTs have a vertical rotor axis, which allows them to capture wind from any direction without the need for reorientation. This feature makes them particularly suitable for locations with variable and turbulent wind patterns. In contrast, HAWTs have a horizontal rotor axis aligned parallel to the ground. To maximize efficiency, HAWTs must be oriented toward the wind using a yaw system, which increases mechanical

complexity but also enhances power capture.

- **Location of the Generator:** In VAWTs, the generator and gearbox are typically positioned at the base of the turbine. This configuration simplifies maintenance procedures and reduces the need for costly lifting equipment. On the other hand, HAWTs position the generator at the top of the tower, allowing access to stronger winds at higher altitudes. However, this setup complicates maintenance due to the elevated location of the components.

- **Wind Direction Dependency:** VAWTs are omnidirectional, meaning they do not need to be aligned with the wind direction, which is an advantage in environments with frequent changes in wind direction or turbulence. In contrast, HAWTs rely on an active yaw system to align the rotor with the wind. Although this adds to the turbine's mechanical complexity, it improves its ability to capture energy from the wind, increasing overall efficiency.

- **Efficiency:** VAWTs generally exhibit lower efficiency compared to HAWTs, especially at higher wind speeds. Nevertheless, they can perform better in environments characterized by low or turbulent winds. HAWTs, by comparison, are more efficient in steady and strong wind conditions, making them the preferred option for large-scale wind energy production.

- **Installation Environment:** VAWTs are better suited for urban or constrained environments where space is limited and wind direction is unpredictable. Their ability to capture wind from any direction makes them ideal for such conditions. Conversely, HAWTs are more appropriate for large open spaces or offshore locations, where wind patterns are more consistent and the turbines can take advantage of higher wind speeds.

- **Height and Size:** VAWTs are typically smaller and installed closer to the ground, which limits their ability to capture wind energy due to lower wind speeds at these heights. In contrast, HAWTs are mounted on taller towers, allowing them to access stronger, more consistent winds at higher altitudes, which leads to a greater energy output.

- **Power Output and Use Case:** Due to their lower power output, VAWTs are commonly employed in small-scale energy applications, such as residential or urban settings. On the other hand, HAWTs are used in large-scale wind farms, where they generate significant amounts of electricity suitable for commercial power generation.

- **Maintenance Complexity:** VAWTs have simpler maintenance requirements since their key components, such as the generator and gearbox, are located near the ground. This makes maintenance easier and less costly. In contrast,

maintaining HAWTs is more complex and expensive due to the height at which critical components are located, often requiring specialized equipment and procedures.

- **Mechanical Stability:** VAWTs are more susceptible to mechanical stresses in turbulent or high-wind environments, which can affect their operational lifespan. In contrast, HAWTs are typically more mechanically robust and stable in a wide range of wind conditions. Their well-established design supports long-term, large-scale energy production.

- **Visual and Acoustic Impact:** VAWTs are generally quieter and less visually intrusive, making them more suitable for urban environments where aesthetics and noise levels are concerns. In contrast, HAWTs are larger and more visible, often having a greater impact on the landscape. Additionally, they tend to generate more noise due to their larger blades and higher rotational speeds.

1.2   Types of Vertical Axis Wind Turbines

There are several distinct types of Vertical Axis Wind Turbines (VAWTs), each designed with specific characteristics that make them suitable for various applications. Below is a detailed overview of the main types [3, 4]:

- **Savonius Turbine:**
  The Savonius turbine [Fig. 1.2a] is one of the simplest and most easily recognizable VAWT designs. It consists of two or more scooped blades that resemble an "S" shape when viewed from above. This drag-based design operates by capturing the wind in its curved blades, generating rotational force. Although it operates effectively at low wind speeds and does not require orientation into the wind, the Savonius turbine has relatively low efficiency compared to lift-based turbines. It is frequently used in small-scale applications such as water pumping or powering small electrical devices in areas with mild wind conditions. Its simplicity of construction and ease of maintenance are key advantages in rural or off-grid environments.

- **Darrieus Turbine:**
  The Darrieus turbine [Fig. 1.2b] is a lift-based design, often referred to as an "eggbeater" due to its characteristic curved blades. Unlike the Savonius, the Darrieus turbine relies on aerodynamic lift rather than drag, which makes it significantly more efficient, especially in regions with higher wind speeds. This turbine type, however, suffers from a major limitation: it cannot self-start at low wind speeds without external assistance or a hybrid design. Darrieus turbines are well-suited for larger wind farms or locations with consistent and

strong wind, where they can generate substantial amounts of energy. Their high efficiency makes them ideal for commercial energy production, but their maintenance requirements are higher due to their more complex design.

- **H-Darrieus Turbine (Giromill):**
A variant of the traditional Darrieus turbine, the H-Darrieus (also known as Giromill) [Fig. 1.2c] replaces the curved blades with straight, vertical blades, forming an "H" shape. This design simplifies construction and maintenance while maintaining the efficiency benefits of a lift-based system. Although it is slightly less efficient than the curved-blade Darrieus, the H-Darrieus performs better in turbulent wind conditions and offers easier access to key components for repair and maintenance. This design is commonly used in urban environments, where wind turbulence is more prevalent, and simplicity of construction is important.

- **Helical Darrieus Turbine:**
The Helical Darrieus turbine [Fig. 1.2d] represents an advanced version of the standard Darrieus, featuring blades that are twisted in a helical shape. This modification helps to smooth the torque variations that occur as the turbine rotates, resulting in more consistent energy production and reduced mechanical stress on the system. The helical design also improves self-starting capabilities, making it a more practical solution in turbulent or variable wind conditions. These turbines are particularly suitable for urban or offshore installations, where wind conditions are less predictable, and higher reliability is required.

- **Hybrid VAWTs:**
Hybrid VAWTs [Fig. 1.2e] combine elements of both drag-based and lift-based turbine designs to optimize performance across a range of wind speeds. Typically, these systems integrate Savonius blades for self-starting and initial torque generation at low wind speeds, and Darrieus-type blades for higher efficiency at greater wind speeds. This combination allows for increased reliability and power generation, even in regions where wind conditions fluctuate significantly. Though more complex and costly to manufacture, hybrid VAWTs are advantageous in environments where versatility in energy capture is crucial, providing a balanced approach to small and medium-scale power generation.

- **Vortex Turbines:**
Vortex turbines [Fig. 1.2f] represent a novel approach to wind energy generation that eliminates traditional rotating blades. Instead, these turbines generate energy through the oscillation of a vertical mast, using resonance to capture the wind's energy. As wind flows past the mast, it induces oscillations, which are then converted into electrical energy via a generator. Vortex turbines are

nearly silent, require minimal maintenance, and have a low visual impact, making them ideal for urban or residential areas where noise and aesthetics are important considerations. Although this technology holds significant promise, it is still in the developmental stages and not yet widely adopted for large-scale energy production.

(a) Savonius turbine   **(b)** Darrieus turbine   **(c)** H-type Darrieus turbine
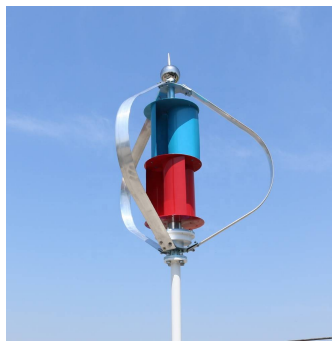
(d) Helical Darrieus turbine   **(e)** Hybrid turbine   **(f)** Vortex turbine

Figure 1.2: Comparison of different turbine types: (a) Savonius, (b) Darrieus, (c) H-type Darrieus, (d) Helical Darrieus, (e) Hybrid, and (f) Vortex turbine.

Chapter 2

Aerodynamic parameters in Vertical Axis Wind Turbines

The aerodynamics of Vertical Axis Wind Turbines (VAWTs) play a crucial role in their efficiency and overall performance. As previously mentioned, VAWTs are designed with rotors that rotate around a vertical axis, which allows them to capture wind from any direction. However, the turbulent wind flow around the rotor results in lower aerodynamic efficiency (30-40%) compared to Horizontal Axis Wind Turbines (50%) [5].

VAWTs are particularly suited for low wind speeds and work at a lower tip speed ratio. The design of the blades, their geometry, and the airfoil profile used are critical factors that significantly affect turbine efficiency. Despite these challenges, VAWTs have the advantage of being structurally simpler, smaller, and lighter than HAWTs.

Several parameters influence the performance of these turbines, including the *rotational speed* ω, the *tip speed ratio* λ, and the Reynolds number. The tip speed ratio λ is defined as the ratio of the tangential speed of the blade to the undisturbed wind speed:

$$\lambda = \frac{R\omega}{V_\infty} \tag{2.1}$$

The Reynolds number is a dimensionless value that represents the ratio between inertial forces and viscous forces within the fluid:

$$Re = \frac{\rho V c}{\mu} \tag{2.2}$$

The power generated by wind turbines can be expressed as:

$$P = C\omega \tag{2.3}$$

8

Where C is the torque produced by the blades, measured in Nm, and ω is the angular velocity of the turbine, measured in rad/s.

This thesis focuses on the study of lift-based wind turbines. In such systems, the driving torque is mainly produced by the lift force, while drag contributes to losses. The structural loads acting on the turbine blades are typically caused by the normal force F_N along the chord of the blade, generated by the aerodynamic forces in the radial direction. The tangential component of the force F_T, on the other hand, is responsible for the torque generated during rotation can be expressed as:

$$C = N_B F_T R \tag{2.4}$$

Where N_B is the number of blades, R is the radius of the turbine, and F_T is the average tangential force during a revolution. If the blades of the turbine are supported by spokes (e.g., H-rotor design), the tangential force also includes the contributions from the blades and the support arms. Both the turbine's geometry and its operating conditions influence the generation of tangential force.

To clarify this aspect, suppose that the blade is positioned at an azimuthal angle θ in the positive counterclockwise direction. The blade's velocity can be expressed as:

$$\vec{V}_{tan} = \Omega R \hat{i} \tag{2.5}$$

Where $\hat{i}$ is the unit vector in the tangential direction in the reference frame fixed to the blade. The relative wind velocity vector $\vec{V}_{rel}$ is the result of the vector sum of the incident wind velocity $\vec{V}_\infty$ and the rotational velocity of the blades, $-\vec{V}_{tan}$ (the negative sign indicates that the flow direction is opposite to the blade rotation).

$$\vec{V}_{rel} = \vec{V}_\infty - \vec{V}_{tan} \tag{2.6}$$

Due to the energy extracted from the flow, the wind speed at the turbine disk, V_{tan}, is generally lower than the freestream velocity, V_∞. In Cartesian coordinates, the magnitude of the relative wind velocity can be calculated as:

$$|\vec{V}_{rel}| = V_\infty \sqrt{1 + \lambda^2 - 2\lambda \cos\theta} \tag{2.7}$$

The angle of attack is the sum of the relative wind angle and the pitch angle δ of the blade (with counterclockwise taken as positive):

$$\alpha = \varphi - \delta \tag{2.8}$$

Assuming $\delta = 0$, the relative angle of attack is calculated as:

$$\varphi = \arctan\left(\frac{\sin\theta}{\frac{\omega R}{V_\infty} + \cos\theta}\right) \tag{2.9}$$

9
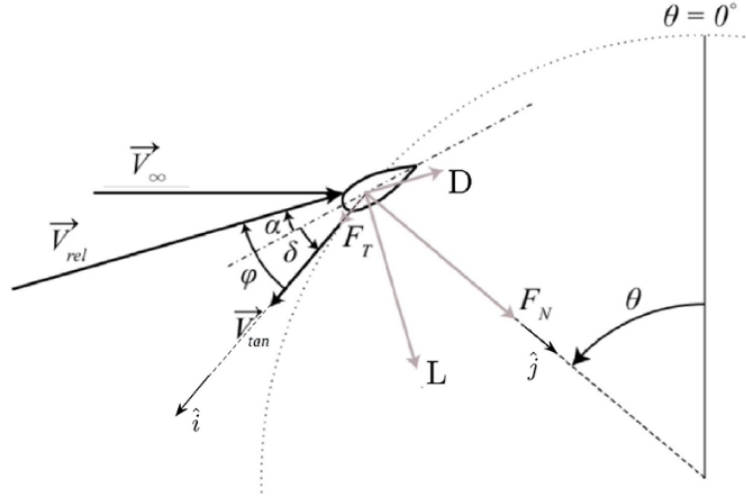
Figure 2.1: Vector velocity diagram and forces acting on a VAWT blade. Positive angles are defined in the counterclockwise direction. The angle φ indicates the relative angle of attack, V_{tan} is the rotational velocity of the blade, and δ is the pitch angle of the blade.

The estimation of the relative angle of attack according to equation (2.9) is valid only if the blade is treated as a point. However, since the blade undergoes rotational motion, it introduces curvature effects that modify the effective angle of attack φ. To account for these curvature effects, the relative wind angle is further modified. From equation (2.9), it can be observed that:

$$\alpha \propto \frac{1}{\lambda} \tag{2.10}$$

To relate this information to the torque generated by the turbine, the expression for the tangential force F_T is given, again assuming $\delta = 0$:

$$F_T = L \sin \alpha - D \cos \alpha \tag{2.11}$$

Here, the lift force $\vec{L}$ is perpendicular to the relative velocity $\vec{V}_{rel}$, while the drag force $\vec{D}$ is parallel to $\vec{V}_{rel}$. From equation (2.11), it can be deduced that the tangential force depends on the blade's angle of attack. As λ increases, there is a reduction in the maximum angle of attack experienced by the blade. As the angle of attack decreases, the drag term becomes more dominant over the lift term, resulting in a lower net tangential force.

10

2.1   Betz's Law

Betz's law defines the maximum power that can be extracted from the wind by a thin, ideal rotor [6]. The theorem makes the following assumptions:

- The rotor has no hub, i.e., it is an ideal rotor with an infinite number of blades and zero friction;

- The flow at the inlet and outlet of the rotor has an axial motion. This type of control volume approach requires that the control volume contain all the incoming and outgoing fluid, in accordance with the conservation equations;

- The fluid is incompressible. The density remains constant, and there is no heat transfer between the rotor and the fluid;

- Apart from the rotor, no other obstacles are present inside the control volume that could alter the fluid motion;

- The portion of the flow that crosses the actuator has no interaction with the remaining part of the fluid that surrounds it and that does not interact with the actuator;

- in the sections upstream and downstream of the rotor, there is a state of absolute aerodynamic calm;

- the fluid velocity is uniformly distributed and has a unidirectional sense in every part of the fluid; no flow reversals are present.
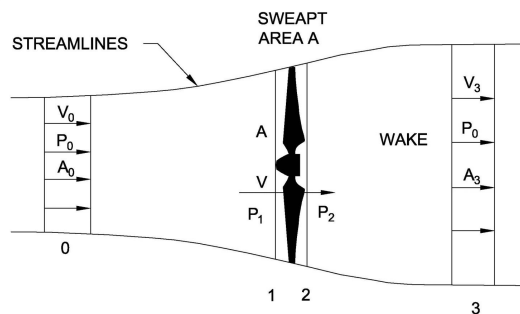
Figure 2.2: Control volume

Applying the continuity equation to the control volume [Fig. 2.2], the fluid flow rate is defined as:

$$\dot{m} = \rho A_1 V_1 = \rho A_2 V_2 \tag{2.12}$$

where V_1 is the upstream velocity, V_2 is the downstream velocity, and V is the velocity on the actuator disk. The force exerted by the fluid on the rotor can be written as:

$$F = \dot{m}\Delta V = \rho S V (V_1 - V_2) \tag{2.13}$$

Writing the work done by the force generated by the rotor:

$$dW = F dx \tag{2.14}$$

and the power contained in the fluid as:

$$P = \frac{dW}{dt} = \frac{F dx}{dt} = FV \tag{2.15}$$

Substituting the force F calculated previously into the power equation, we obtain:

$$P = \rho S V^2 (V_1 - V_2) \tag{2.16}$$

Equating the expression just obtained with that derived from the calculation of the power using kinetic energy, we get:

$$\frac{1}{2}\rho S V (V_1^2 - V_2^2) = \rho S V^2 (V_1 - V_2) \tag{2.17}$$

Therefore, the fluid velocity at the rotor $V = \frac{1}{2}(V_1 + V_2)$ can be considered as the average of the velocities of the upstream and downstream sections, under the condition that these velocities are not equal, in which case no power is extracted. Defining the power coefficient as the ratio between the delivered power and the maximum extractable power, we obtain:

$$C_p = \frac{P}{P_{max}} \tag{2.18}$$

To obtain this value, we start from the previous expression of power based on kinetic energy:

$$E = \frac{1}{2}m(V_1^2 - V_2^2) = \frac{1}{4}\rho S V^3 \left(1 - \left(\frac{V_2}{V_1}\right)^2\right) \tag{2.19}$$

In particular, the maximum of the function E occurs for $\frac{V_2}{V_1} = \frac{1}{3}$. From this, we obtain the maximum fraction of work extractable from the flow:

$$P = \frac{16}{27}\rho SV_1^3 \tag{2.20}$$

While the fraction of work made available by a fluid cylinder with an area in the disk section of the rotor S and velocity V_1 is:

$$P_{max} = \frac{1}{2}\rho SV_1^3 \tag{2.21}$$

Therefore, the power coefficient is:

$$C_{p,max} = 0.593 \tag{2.22}$$

It is important to remark that Betz's limit is valid for horizontal axis wind turbines. In order to apply the law to other types of turbines, it needs to be corrected accordingly to the geometry that needs to be evaluated. In Fig. 2.3 are summarized the power coefficient curves for the main configurations.
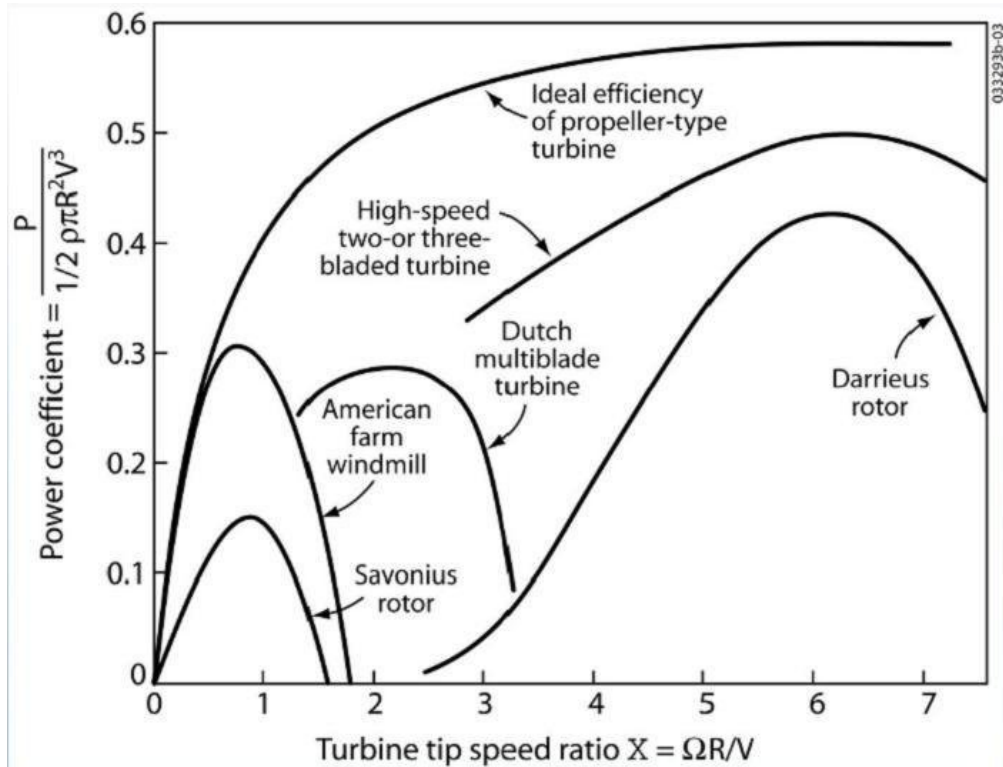
Figure 2.3: Betz's limit for different types of turbines

13

2.2 Effects of flow curvature

Equation (2.9), presented in the previous section, is reported here for ease of reading:

$$\varphi = \arctan\left(\frac{\sin\theta}{\frac{\Omega R}{V_\infty} + \cos\theta}\right) \tag{2.23}$$

This expression is valid only for infinitely thin symmetric blades. The blade of a vertical axis wind turbine undergoes a rotational motion, which leads to further flow curvature, modifying the effective angle of attack.

The curved flow field of Darrieus turbines can be studied using conformal mapping techniques as done by Deglaire [7]. With this method, the real (geometric) profile in the curved flow can be transformed into an equivalent (virtual) profile in a rectilinear flow. With this approach, local velocities and angles of attack are preserved, so that the virtual profile shows the aerodynamic behavior of the rotating geometric profile.
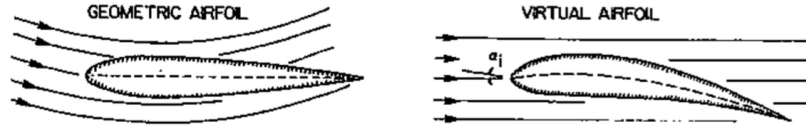
Figure 2.4: Curvature effects on an airfoil

Migliore [8] studied the effect of virtual camber resulting from flow curvature for an NACA0015 profile used on a Darrieus turbine. Within this study, it was assumed that the symmetric profile was mounted at the quarter chord with a zero camber ($\delta = 0$), and an undisturbed flow velocity $V_\infty = \infty$ was considered in order to eliminate the dependence of the angle of incidence on the azimuthal position. The analyses showed how the effects of flow curvature introduced an effective angle of incidence in addition to the normal angle experienced by the blade along the rotation, noting how the shape of the profile itself was altered. The results obtained by Migliore highlighted how the effects of virtual incidence and virtual camber were strongly dependent on the geometric parameter c/R (blade chord to turbine radius ratio). Based on conformal mapping, Goude [9] proposed a more accurate formulation of the angle of incidence experienced by the blades of a Darrieus turbine due to flow curvature:

$$\beta = \theta + \arctan\left(\frac{\sin\theta}{\cos\theta + \frac{\Omega r_c}{V_\infty}}\right) \tag{2.24}$$

14

where θ is the azimuthal position of the blade, Ω is the angular velocity of the turbine in rad/s, r_c is the distance in meters between the leading edge of the profile and the attachment to the turbine arm, c is the blade chord in meters, and V_∞ is the undisturbed flow velocity in m/s.

2.3 Dynamic Stall in Vertical Axis Wind Turbines (VAWTs)

Dynamic stall is a complex aerodynamic phenomenon that occurs when a blade experiences rapid changes in the angle of attack, leading to transient effects on the generation of lift and drag forces. In Vertical Axis Wind Turbines (VAWTs), dynamic stall plays a critical role, especially at low Tip Speed Ratios (TSR) or when operating in turbulent wind conditions.

While static stall occurs when the angle of attack exceeds a critical threshold, causing a steady loss of lift due to flow separation, dynamic stall is a more transient and time-dependent event. It is characterized by the formation and shedding of vortices from the suction side of the blade [10, 11], which can lead to significant unsteady forces. This phenomenon is particularly prevalent in VAWTs, where the blades experience cyclic variations in the angle of attack as they rotate through different phases of the wind.

In a VAWT, each blade encounters a wide range of angles of attack during its rotation. As the blade moves into the wind (upwind phase), the angle of attack increases. If this angle exceeds the critical stall angle, the boundary layer begins to separate from the surface of the blade, leading to a rapid decrease in lift and an increase in drag. However, unlike in static stall, where this separation is relatively stable, dynamic stall involves the shedding and passage of a vortex-like disturbance over the low-pressure surface of the lifting surface. The passage of the vortex over the low-pressure surface of a pitching airfoil produces values of C_l, C_m, and C_d far in excess of their static counterparts during the upstroke. Because this phenomenon results from the combination of the unsteady motion of the airfoil and the separation of the boundary layer, it is affected by parameters related to the airfoil motion (motion type, reduced frequency, maximum angle) and parameters related to the separation of the boundary layer (airfoil shape, Reynolds number, Mach number, and three-dimensional effects). As an example, a chronology of dynamic-stall events and typical hysteresis for C_l, C_m, and C_d versus the angle of attack are depicted in Fig. 2.5. The main phases of this transient phenomenon are listed below:

1. During the fast upstroke motion of the airfoil, the flow stays attached beyond the steady separation point, although reversed flow occurs inside the boundary layer;

2. During the high incidence range of the upstroke motion, a dynamic-stall vortex develops at the airfoil leading edge and moves over the upper surface with about 22% of the undisturbed mainflow velocity,This vortex remains attached to the blade for a short time, generating a temporary increase in lift, which is referred to as the "dynamic stall lift overshoot";

3. The vortex lifts off the airfoil and is shed into the wake. As the vortex detaches and moves downstream, the lift decreases sharply, leading to a dramatic shift in the forces acting on the blade;

4. A counter-rotating vortex originates from the trailing edge and interacts with the primary vortex;

5. Weaker secondary and higher order vortices start either from the leading edge (clockwise) or trailing edge (anti-clockwise) during the downstroke motion;

6. Reattachment of the flow from leading to trailing edge occurs very late in the cycle, during downstroke [12].
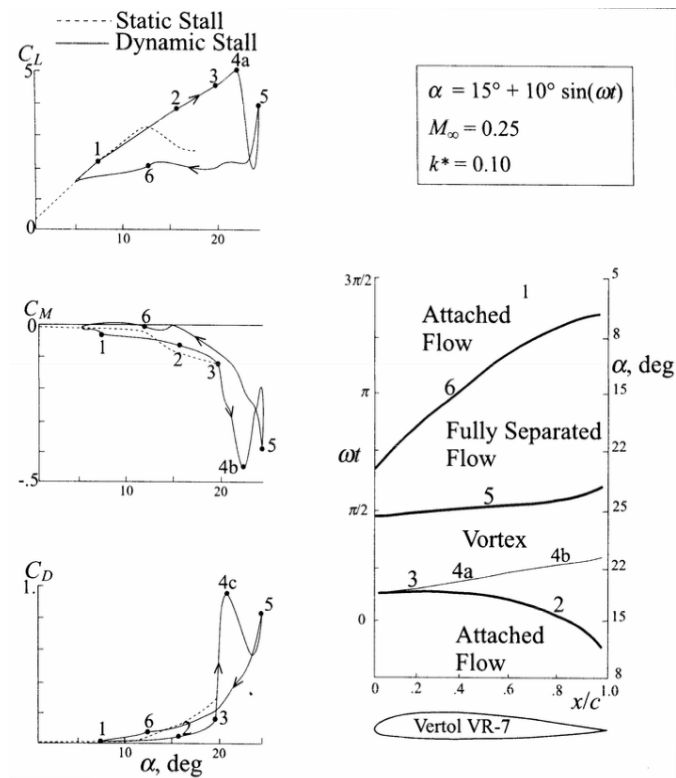
Figure 2.5: Dynamic stall phases on a Vertol VR-7 airfoil

16

It is obvious that the dynamic effects of the airfoil motion as well as the dynamics of the different vortices influence the overall forces and moments acting on the airfoil [13]. The oscillations in lift and drag caused by dynamic stall lead to unsteady aerodynamic loads, which can result in increased fatigue and vibration of the turbine structure. These fluctuating loads are especially pronounced in Darrieus-type VAWTs, where the blades move through large variations in the relative wind velocity and angle of attack during each rotation [14]. Dynamic stall can significantly affect the performance of VAWTs, as the unsteady aerodynamic forces reduce the overall efficiency of the turbine. The lift overshoot associated with dynamic stall can momentarily increase the power output of the turbine, but this is followed by a sharp decline as the stall fully develops. This results in a non-uniform torque distribution and fluctuations in power generation, making it difficult to maintain optimal operational performance.

Moreover, the unsteady forces generated by dynamic stall impose additional structural loads on the turbine blades and supporting components. The rapid changes in aerodynamic forces can cause high-cycle fatigue, leading to material degradation and potentially reducing the lifespan of the turbine. Therefore, mitigating the effects of dynamic stall is essential for improving both the performance and durability of VAWTs.

Several strategies have been proposed to mitigate the effects of dynamic stall in Vertical Axis Wind Turbines (VAWTs):

- Optimizing the blade design: A study conducted by Hoerner et al. focuses on blade design and the impact of bioinspired flexible blade profiles, aiming to enhance aerodynamic performance in turbines. This study highlights how aerodynamic optimization of the airfoil shape and pitch angle can reduce flow separation and improve overall efficiency by delaying stall onset [15].

- Controlling the angle of attack through the use of variable-pitch blades: Research on dynamic stall control, such as the study by Zhou et al., explores how varying pitch angles during blade rotation reduces unsteady loads and improves performance by controlling the angle of attack [16].

- Placement of vortex generators or flow control devices: The work by Yen and Ahmed demonstrates how using synthetic jets as active flow control can delay the onset of dynamic stall, thus reducing its intensity. Vortex generators are an effective method to control flow separation on the blades [17].

Chapter 3

Numerical Simulation Models

The study of the flow around a VAWT turbine requires a thorough analysis of the turbulence phenomena generated by the rotational motion of the blades and by the interaction of the same with the wake produced by the rotor. In turbulent motion, local variables fluctuate chaotically over time, with a very high frequency of about 100-1000 Hz around a mean value that varies much more slowly. Assuming that the turbulent oscillation period τ_e is significantly lower than the characteristic evolution times of the system τ_s, it is possible to decompose the generic variable $\phi(t)$ into a mean component and a fluctuating one (with zero mean value):

$$\phi(t) = \overline{\phi}(t) + \phi'(t) \tag{3.1}$$

To characterize the fluctuations, their root mean square is used, so the turbulence intensity for a component $k = x, y, z$ is obtained from:

$$i_k = \frac{\sqrt{\overline{v_k'^2}}}{\overline{v_k}} \tag{3.2}$$

The overall turbulence intensity is written as:

$$i = \sqrt{\frac{v_x^2 + v_y^2 + v_z^2}{3}} \tag{3.3}$$

Therefore, the turbulent kinetic energy:

$$K = \frac{1}{2}(i\overline{v})^2 \tag{3.4}$$

and finally, the cross-correlation parameter that expresses the degree of covariance between the two quantities, i.e., how much a variation in the velocity in the direction i is associated with a variation in the velocity in the j direction:

$$c_{ij} = \overline{v'_i v'_j} \tag{3.5}$$

In turbulence, the generation of vortices is observed, i.e., the formation of structures where the fluctuating variables remain correlated:

$$c_{ij} \neq 0 \tag{3.6}$$

These structures can have different dimensions, and the larger their dimensions, the longer their lifetime.

It is possible to define different scales of magnitude, from the dimension of the duct where the flow develops to that of Kolmogorov. Kolmogorov scales are the smallest scales used in the description of a turbulent flow. In his 1941 theory, Andrey Nikolaevich Kolmogorov introduced the idea that the smallest scales to which turbulence can be described are universal, i.e., similar for any turbulent flow, independently of the physical phenomenon that generated it, and dependent only on the two parameters ν and ϵ. Since turbulence is the transfer of turbulent kinetic energy from the largest to the smallest eddies, the numerical study of turbulence involves the use of different techniques depending on the scale of the vortex that one intends to resolve.

All numerical models are based on the solution of the Navier-Stokes equations, which in Cartesian coordinates and in indicial form can be written as:

$$\frac{\partial \rho}{\partial t} + \frac{\partial (\rho u_j)}{\partial x_j} = 0 \tag{3.7}$$

$$\frac{\partial (\rho u_i)}{\partial t} + \frac{\partial (\rho u_i u_j)}{\partial x_j} = -\frac{\partial p}{\partial x_i} + \frac{\partial \tau_{ij}}{\partial x_j} \tag{3.8}$$

$$\frac{\partial (\rho E)}{\partial t} + \frac{\partial (\rho H u_j)}{\partial x_j} = \frac{\partial}{\partial x_j} \left(\tau_{ij} u_i - q_j \right) \tag{3.9}$$

Equation 3.7 represents the continuity equation, equation 3.8 the conservation of momentum, and equation 3.9 the conservation of energy in the system. These equations describe the evolution over time of the velocity field of the fluid, taking into account the forces that act on it. These equations are very complex and often require the use of numerical simulation techniques to be solved, and a frequent application is found in aerodynamic simulations.

19

3.1 Direct Numerical Simulation

DNS simulations directly use the numerical integration of the Navier-Stokes equations. This approach is absolutely the most accurate but involves very high computational costs, due to the need to resolve the problem at all scales of length. In particular, the DNS method provides a discretization of space-time in a way to transform the differential form of the Navier-Stokes equations into a system of algebraic equations that can be solved through numerical computation. The method requires a very fine mesh, with spatial resolution inferior to the Kolmogorov scale, to capture the smallest details of the turbulent flow. This means that the number of grid nodes necessary for a DNS simulation can become very large and require an enormous computational capacity. The advantage of DNS is that it provides a detailed and accurate description of the flow properties, of turbulent phenomena, of mass and heat exchange coefficients, and of other quantities important for engineering and scientific research.

However, due to the high computational cost, DNS is generally limited to flows at low velocity and to relatively simple geometries. In summary, DNS is a powerful tool for detailed and accurate numerical simulations of the behavior of fluids, but it requires an enormous computational capacity and a the grid must be fine enough to capture the details of the turbulent flow. Moreover, the spatial spacing Δx of the computational grid must be small enough to be able to resolve the dissipative scales of the flow (Kolmogorov scales). Therefore, the time-step Δt used is limited by the numerical accuracy obtaining an estimate of the Courant number as: $k\Delta t/\Delta x = 1/20$.

3.2 Large Eddy Simulation

This approach allows to overcome the computational cost due to the integration over small scales by resolving the motion only at the length and time scales of the large vortices that interact significantly with the mean motion; at smaller scales, where the turbulence has characteristic "universal" scales, additional constitutive models, based on the turbulent viscosity are used.

In this type of numerical analysis, the Navier-Stokes equations for the conservation of mass and momentum are solved; a filter is necessary to separate the scales resolved from those not resolved. If the equations are discretized using a finite difference scheme, the filter is usually applied implicitly using a box-filter coincident with the computational grid. If instead a spectral method is used for the solution of the numerical equations it is necessary to apply explicitly a sharp-cutoff filter defined in the Fourier space.

The LES numerical simulation technique requires a high number of cells in proximity of the wall, a factor that often limits its applicability in external aerodynamics where the use of models based on the Reynolds Averaged Navier-Stokes equations (RANS) is the most adequate. However, the LES approach is a common choice in contexts in which RANS is not effective, such as for example in the simulation of combustion processes, mixing of fluids or flows around bodies with complex geometry.

3.3   Reynolds-Averaged Navier-Stokes methods

RANS are based on the concept of averaging the fluid properties in time and space and are used to predict the mean values of the properties of turbulent flows. Despite their limitations, they are widely used thanks to the low computational costs compared to those of LES and DNS.

The RANS equations are obtained by introducing the Reynolds decomposition:

$$\vec{u} = \vec{U} + \vec{u}', \quad p = P + p' \tag{3.10}$$

where the terms u' and p' represent the fluctuating terms, while U and P are the mean values of velocity and pressure respectively. Substituting in equations (2.7) and (2.8) and averaging, we obtain:

$$\frac{\partial U_i}{\partial x_i} = 0 \tag{3.11}$$

$$\frac{\partial U_i}{\partial t} + U_j \frac{\partial U_i}{\partial x_j} = -\frac{1}{\rho}\frac{\partial P}{\partial x_i} + \nu \frac{\partial^2 U_i}{\partial x_j \partial x_j} - \frac{\partial}{\partial x_j}\overline{u_i'u_j'} \tag{3.12}$$

The term $-\overline{u_i'u_j'}$ is known as the Reynolds stress tensor and its divergence appears as a volumetric force. The RANS methods require the use of closure equations to determine this term. A first approach was proposed by Joseph Valentin Boussinesq based on the eddy viscosity hypothesis (eddy viscosity). According to this hypothesis the Reynolds stress is proportional to the mean rate of deformation tensor through the turbulent viscosity:

$$-\rho\overline{u_i'u_j'} + \frac{2}{3}k\delta_{ij} = -\rho a_{ij} = \rho\nu_t\left(\frac{\partial U_i}{\partial x_j} + \frac{\partial U_j}{\partial x_i}\right) = 2\rho\nu_t\overline{S_{ij}} \tag{3.13}$$

where $k = \frac{1}{2}\overline{u_i'u_i'}$ is the turbulent kinetic energy per unit mass, $\overline{S_{ij}}$ is the mean rate of deformation tensor, and a_{ij} is the anisotropy tensor, and $\nu_t(x,t)$ is the turbulent viscosity. Subsequently, Taylor and Prandtl introduced the concept of the mixing length; this arises from the application of Boussinesq's theory to the boundary layer:

$$\nu_t(x, y) = l^*(x, t) \cdot u^*(x, t) \tag{3.14}$$

From these theories, one-equation and two-equation closure models arise.

3.4 Spalart-Allmaras Model

The Spalart-Allmaras model uses a transport equation for the turbulent viscosity. The authors of the original Spalart-Allmaras turbulence model have presented results for attached boundary layers and flows with a slight separation. It is reasonable to expect that these cases are the types of flows for which the model provides the best results.

3.5 Turbulence Models

3.5.1 k-ε Model

The k-ε model is a two-equation model that solves transport equations for the turbulent kinetic energy k and the dissipation rate ε to determine the turbulent viscosity. This model presents good results for simple flows but performs poorly for flows with severe adverse pressure gradients, separation, and complex flow patterns.

3.5.2 k-ω Model

The k-ω model is a two-equation turbulence model that solves transport equations for the turbulent kinetic energy k and the specific dissipation rate ω. An advantage of the k-ω model with respect to the k-ε model is the improvement of the performance for boundary layers in presence of adverse pressure gradients. Moreover, the k-ω model can be applied to the full viscous layer, without modifications. However, the standard k-ω model presents the disadvantage of particular sensitivity to the wall distance in the near-wall region, which requires particular refinement of the near-wall cells. This issue is particularly evident in internal flows conditions imposed at the inlet, for instance, and it causes an extreme sensitivity to the k and ω values at the far-field. Original k-ω models in the shear stress limit are sensitive to 1 value of ω at the inlet. In STAR-CCM+, some modifications have been made in an attempt to solve this problem.

3.5.3 Reynolds Stress Models

Reynolds Stress Models (RSM) are based on the Reynolds stress tensor. Physically, they are the most solid RANS model. They avoid the Boussinesq assumption.

RSM require a higher computational cost, as they solve seven equations at each iteration. They have a more difficult convergence due to the strong coupling of the equations. These models are very suitable for three-dimensional complex flows with strong curvature of streamlines, high vorticity/rotation (e.g., curved ducts, rotating flows, combustors with very large inlet vortices, cyclones).

3.6 Turbulence Models in VAWT CFD Simulations

The simulation of a Vertical Axis Wind Turbine (VAWT) using Computational Fluid Dynamics (CFD) presents significant challenges due to the complex flow dynamics involved. The choice of turbulence model is critical, as it influences the accuracy and computational efficiency of the simulation. One commonly used approach in wind turbine simulations is based on the Reynolds-Averaged Navier-Stokes (RANS) equations. These models provide a good balance between computational cost and the ability to capture time-averaged turbulent flow characteristics.

For VAWT simulations, RANS models are often preferred due to their computational efficiency and their capacity to provide reasonably accurate results for time-averaged turbulent flows. Two of the most widely used RANS models are the k-ε and k-ω models. In reviewing the literature, it appears that no single model has a clear advantage over the other, as the choice often depends on the specific flow conditions and the goals of the simulation.

Among the k-ε models, the Realizable k-ε model is the most frequently employed [18, 19, 20, 21]. It is known for its robust performance and ease of convergence in most cases. However, other variations such as the standard k-ε model [22] and the RNG (Re-Normalization Group) k-ε model [23, 24] have also been used in studies, demonstrating their applicability in specific flow scenarios.

On the other hand, the k-ω models are often considered more reliable in theory, particularly for simulations involving adverse pressure gradients and complex separation phenomena. Their capability to predict flow separation with greater accuracy makes them advantageous in highly turbulent environments, such as those encountered in VAWT simulations. The standard k-ω model [25] is commonly used, but it is often supplemented by more advanced models such as the SST (Shear Stress Transport) k-ω model [26, 27] and the SST-SAS (Scale-Adaptive Simulation) k-ω model [28].

The SST k-ω model is particularly noteworthy because it blends the strengths of the k-ε and k-ω models, using the k-ω formulation near the walls for improved boundary layer accuracy, while switching to k-ε in the far-field to avoid excessive sensitivity to free-stream turbulence. This hybrid approach provides a more accurate prediction of flow separation and turbulence characteristics, making it a

popular choice in wind turbine simulations. The SST-SAS model goes even further by introducing scale-adaptivity, allowing the model to capture unsteady, large-scale structures in the flow field without fully transitioning to a computationally expensive Large Eddy Simulation (LES) approach. This makes it suitable for VAWT simulations where unsteady effects play a critical role in the overall turbine performance.

The specific merits and limitations of the SST k-ω model will be discussed in more detail in the following chapter.

LES simulations are another option that can be used to simulate structures on a large scale [29]. Large-eddy simulation (LES) is a possible simulation procedure to simulate VAWT. LES models are in general more accurate but more computationally expensive than RANS models. In general, RANS models, including RST or SST models, are more suitable for VAWT simulations than LES models. Due to the complexity of VAWT flow dynamics and the computational resources required to resolve all the scales of the flow, VAWT RANS models are computationally more accurate and utilized to provide a good compromise between efficiency and computational accuracy.

It is important to note that the choice of the turbulence model for a specific simulation is also influenced by other parameters, such as the turbulence intensity, the type of boundary conditions, the grid resolution, the numerical scheme, and the validity of the hypotheses of the turbulence model and may require some trial and error.

Chapter 4

The Turbulence Model

In aerodynamic simulations, solving the Navier-Stokes equations is essential for addressing complex turbulent flows, particularly where inviscid or viscous-inviscid interaction methods fall short. Such cases typically include flows with extensive separations, varying length scales, three-dimensional flow separation, and strong unsteady behavior. Traditional algebraic turbulence models, such as those developed by Cebeci-Smith, Baldwin-Lomax, and Johnson-King, face challenges due to their reliance on predefined algebraic length scales. With the advancement of computational fluid dynamics (CFD), there arose a need for more flexible turbulence models compatible with Navier-Stokes solvers.

A robust turbulence model must not only eliminate dependency on fixed length scales but also maintain accuracy, numerical stability, and computational efficiency. Additionally, it should minimize the reliance on uncertain external inputs, like freestream values.

Two-equation eddy-viscosity models, which solve transport equations for turbulent kinetic energy (k) and a related scale, are widely used. The k-ε model is particularly common, and its low-Reynolds-number version, developed by Jones and Launder, has found significant use. However, in aerodynamic flows, this model often encounters difficulties when dealing with adverse pressure gradients, leading to delayed or missed predictions of flow separation due to overestimating turbulent length scales in near-wall regions. Although modifications, such as those suggested by Hanjalic and Launder, have improved performance in certain situations, these adjustments lack universal applicability, particularly for complex geometries. Moreover, the k-ε model tends to exhibit numerical stiffness in the viscous sublayer, complicating convergence.

To address these challenges, Wilcox introduced the k-ω model, which computes both the turbulent kinetic energy (k) and the specific dissipation rate (ω). This model shows better performance in adverse pressure gradient conditions and avoids the need for damping functions in the viscous sublayer, resulting in improved

numerical stability. However, a drawback of the k-ω model is its sensitivity to the freestream value of ω, which can cause significant variability in the predicted eddy-viscosity and reduce consistency.

Menter proposed the Baseline (BSL) k-ω model to mitigate this sensitivity. By blending between k-ω near walls and k-ε in shear layers, this model retains the strengths of both while reducing freestream dependency.

Later, Menter developed the Shear Stress Transport (SST) model [30], further enhancing performance in flows with strong adverse pressure gradients. Inspired by the Johnson-King model, the SST model introduces modifications to the eddy-viscosity formulation to account for the transport of turbulent shear stresses. This results in more accurate flow separation predictions and better overall numerical stability, without significantly increasing computational cost.

The SST model offers several advantages, such as improved accuracy in predicting flow separation and enhanced stability, while maintaining compatibility with Wilcox's modifications for rough surfaces and wall functions. This makes it an effective and versatile model for various aerodynamic flow scenarios.

4.1 The Shear-Stress Transport (SST) Model

The core concept behind the SST model is to integrate the accurate near-wall performance of the Wilcox k-ω model with the freestream insensitivity of the k-ε model in the outer regions of the boundary layer. This is achieved by reformulating the k-ε model into a k-ω framework and introducing a cross-diffusion term into the ω equation. The model constants are also adjusted for consistency.

To blend these two models, a blending function F_1 is used. The original k-ω model is multiplied by F_1, while the transformed k-ε model is multiplied by $(1-F_1)$. The two contributions are then summed, with F_1 set to 1 near walls and 0 farther from the surface, creating a smooth transition between models in the boundary layer's wake region. In the following equations, D/Dt represents the Lagrangian derivative, expressed as $D/Dt = \partial/\partial t + u_i \partial/\partial z_i$.

$$\frac{Dk}{Dt} = \tau_{ij} \frac{\partial u_i}{\partial z_j} - \beta^* \rho k \omega + \frac{\partial}{\partial z_j} \left[(\mu + \sigma_{k1} \mu_t) \frac{\partial k}{\partial z_j} \right] \tag{4.1}$$

$$\frac{D\omega}{Dt} = \frac{\gamma_1}{\nu_t} \tau_{ij} \frac{\partial u_i}{\partial z_j} - \beta_1 \rho \omega^2 + \frac{\partial}{\partial z_j} \left[(\mu + \sigma_{\omega1} \mu_t) \frac{\partial \omega}{\partial z_j} \right] \tag{4.2}$$

For the modified k-ε model:

$$\frac{Dk}{Dt} = \tau_{ij} \frac{\partial u_i}{\partial z_j} - \beta^* \rho k \omega + \frac{\partial}{\partial z_j} \left[(\mu + \sigma_{k2} \mu_t) \frac{\partial k}{\partial z_j} \right] \tag{4.3}$$

26

$$\frac{D\omega}{Dt} = \frac{\gamma_2}{\nu_t}\tau_{ij}\frac{\partial u_i}{\partial z_j} - \beta_2\rho\omega^2 + \frac{\partial}{\partial z_j}\left[(\mu + \sigma_{\omega 2}\mu_t)\frac{\partial\omega}{\partial z_j}\right] + 2\rho\left(1 - F_1\right)\sigma_{\omega 2}\frac{1}{\omega}\frac{\partial k}{\partial z_j}\frac{\partial\omega}{\partial z_j} \quad (4.4)$$

The blending procedure involves multiplying equations (4.1) and (4.2) by F_1, and equations (4.3) and (4.4) by $(1 - F_1)$, and summing the results:

$$\phi = F_1\phi_1 + (1 - F_1)\phi_2 \quad (4.5)$$

Here, ϕ_1 corresponds to the constants of the original k-ω model, adjusted to recover the correct behavior in boundary-layer flows, and ϕ_2 represents the constants of the transformed k-ε model. The values for the constants are:

Set 1 (ϕ_1) modified from Wilcox:

$$\sigma_{k1} = 0.85, \quad \sigma_{\omega 1} = 0.5, \quad \beta_1 = 0.0750, \quad a_1 = 0.31,$$
$$\beta^* = 0.09, \quad \kappa = 0.41, \quad \gamma_1 = \beta_1/\beta^* - \sigma_{\omega 1}k^2/\sqrt{\beta^*} \quad (4.6)$$

Set 2 (ϕ_2) from the standard k-ε model:

$$\sigma_{k2} = 1.0, \quad \sigma_{\omega 2} = 0.856, \quad \beta_2 = 0.0828,$$
$$\beta^* = 0.09, \quad \kappa = 0.41, \quad \gamma_2 = \frac{\beta_2/\beta^* - \sigma_{\omega 2}\kappa^2}{\sqrt{\beta^*}} \quad (4.7)$$

The near-wall region applies set (4.6), while the outer boundary layer and shear layers use set (4.7).

A critical difference between the eddy-viscosity models and full Reynolds-stress models, particularly in aerodynamic applications, is the ability of the latter to model the transport of turbulent shear stresses. The primary shear stress is expressed as:

$$\tau = -\rho\overline{u'v'} \quad (4.8)$$

This transport is integrated into the SST model through the following equation:

$$\frac{D\tau}{Dt} = \frac{\partial\tau}{\partial t} + u_k\frac{\partial\tau}{\partial x_k} \quad (4.9)$$

The importance of this term is supported by the success of models like Johnson-King (JK), which outperform simpler models by incorporating turbulent shear-stress transport in adverse pressure gradient flows.

The SST model uses Bradshaw's assumption that turbulent shear stress is proportional to turbulent kinetic energy k, formulated as:

$$\tau = \rho a_1 k \tag{4.10}$$

where a_1 is a constant. In two-equation models, the shear stress can be written as:

$$\tau = \mu_t \Omega \tag{4.11}$$

where $\Omega = \frac{\partial u}{\partial y}$ is the shear strain rate. For most models, this can be redefined as:

$$\tau = \rho \sqrt{\frac{Production_k}{Dissipation_k}} a_1 k \tag{4.12}$$

In adverse pressure gradient flows, the production-to-dissipation ratio can become significantly greater than 1, leading to overestimation of τ. To correct this, the eddy-viscosity is defined as:

$$\nu_t = \frac{a_1 k}{\Omega} \tag{4.13}$$

This adjustment ensures that τ does not increase excessively with $\rho a_1 k$. In adverse pressure gradients, where production exceeds dissipation, the eddy-viscosity is further modified as:

$$\nu_t = \frac{a_1 k}{\max(a_1 \mu, \Omega)} \tag{4.14}$$

This ensures that ν_t is appropriately computed for regions with adverse pressure gradients. In the remainder of the boundary layer, it can be represented as:

$$\nu_t = \frac{\mu_t}{\rho} = \frac{k}{\omega} \tag{4.15}$$

The blending function F_2 is introduced to localize the model to wall-bounded flows, similar to the BSL model. The eddy-viscosity is now expressed as:

$$\nu_t = \frac{a_1 k}{\max(a_1 \omega; \Omega F_2)} \tag{4.16}$$

To complete the model, the blending function F_1 is defined based on the argument:

$$arg = \max\left(\sqrt{\frac{k}{0.09\omega y}}, \frac{500\nu}{y^2 \omega}\right) \tag{4.17}$$

The Shear Stress Transport (SST) model combines the strengths of the k-ω model near the wall and the k-ε model in the outer flow. This hybrid approach

28

ensures accurate predictions for a wide range of flow types, especially those involving boundary layers under adverse pressure gradients.

The SST model works by transforming the k-ε model into a k-ω form, modifying constants, and introducing a cross-diffusion term in the ω equation. A blending function F_1 is used to transition between the two models, where $F_1 = 1$ near the wall (activating the k-ω model) and $F_1 = 0$ in the freestream, activating the modified k-ε model in the outer region. The Lagrangian derivative $\frac{D}{Dt}$ captures changes in time and space, representing the movement of fluid particles.

Key equations governing the SST model include:

- For the k-ω model:

$$\frac{Dk}{Dt} = \tau_{ij}\frac{\partial u_i}{\partial z_j} - \beta^* \rho k \omega + \frac{\partial}{\partial z_j}\left[(\mu + \sigma_{k1}\mu_t)\frac{\partial k}{\partial z_j}\right]$$

$$\frac{D\omega}{Dt} = \frac{\gamma_1}{\nu_t}\tau_{ij}\frac{\partial u_i}{\partial z_j} - \beta_1 \rho \omega^2 + \frac{\partial}{\partial z_j}\left[(\mu + \sigma_{\omega 1}\mu_t)\frac{\partial \omega}{\partial z_j}\right]$$

- For the transformed k-ε model:

$$\frac{Dk}{Dt} = \tau_{ij}\frac{\partial u_i}{\partial z_j} - \beta^* \rho k \omega + \frac{\partial}{\partial z_j}\left[(\mu + \sigma_{k2}\mu_t)\frac{\partial k}{\partial z_j}\right]$$

$$\frac{D\omega}{Dt} = \frac{\gamma_2}{\nu_t}\tau_{ij}\frac{\partial u_i}{\partial z_j} - \beta_2 \rho \omega^2 + \frac{\partial}{\partial z_j}\left[(\mu + \sigma_{\omega 2}\mu_t)\frac{\partial \omega}{\partial z_j}\right] + 2\rho\left(1 - F_1\right)\sigma_{\omega 2}\frac{1}{\omega}\frac{\partial k}{\partial z_j}\frac{\partial \omega}{\partial z_j}$$

Blending these two models results in an effective equation:

$$\phi = F_1\phi_1 + (1 - F_1)\phi_2$$

Where ϕ_1 corresponds to the k-ω model's parameters, and ϕ_2 aligns with the transformed k-ε model. Constants such as σ_{k1}, β_1, γ_1 for the k-ω model, and σ_{k2}, β_2, γ_2 for the k-ε model are tailored to ensure the correct behavior across the boundary layer.

The SST model includes a crucial component: the calculation of turbulent shear stress τ, which is based on the turbulent kinetic energy k, expressed as:

$$\tau = \rho a_1 k$$

In this context, a_1 is a constant. The relationship between turbulent shear stress and eddy viscosity ν_t is also considered, and it adapts based on different regions of the flow. For instance, in adverse pressure gradient conditions, production of turbulence exceeds dissipation, leading to modifications in the eddy viscosity term.

To handle the adverse pressure gradient, the eddy viscosity is redefined as:

$$\nu_t = \frac{a_1 k}{\Omega}$$

where Ω represents the shear-strain rate. In boundary layers with a strong adverse pressure gradient, the model adjusts further to prevent over-prediction:

$$\nu_t = \frac{a_1 k}{\max(a_1 \mu, \Omega)}$$

The SST model smoothly transitions between the k-ω and k-ε regions using blending functions like F_1 and F_2, with the argument defined as:

$$arg = \max\left(\sqrt{\frac{k}{0.09\omega y}}, \frac{500\nu}{y^2 \omega}\right)$$

The overall formulation ensures robustness in complex flows, particularly where boundary layers are affected by pressure gradients. By combining the best features of the k-ω and k-ε models, the SST model provides greater accuracy in predicting turbulent flows without requiring prior knowledge of the flow zones.

4.2   Boundary Conditions

For wall-bounded flows, at a no-slip boundary, all turbulent quantities, except ω, are set to zero. As noted by Wilcox, ω behaves as follows near the wall:

$$\omega = \frac{6\nu}{\beta_1 y^2} \quad \text{as} \quad y \to 0 \tag{4.18}$$

Wilcox recommends that this analytical solution should be specified for the first few grid points near the wall. However, in practice, it is simpler and equally accurate to impose the boundary condition:

$$\omega = \frac{10\nu}{\beta_1 (\Delta y)^2} \quad \text{at} \quad y = 0 \tag{4.19}$$

Here, Δy is the distance to the nearest grid point from the wall. Equation (4.19) serves as a substitute for equation (4.18), ensuring a smooth transition without the need for adjusting the solution at internal points. It is essential to note that the k-ω equation delivers accurate results if ω values near the wall are sufficiently large. Both equations (4.18) and (4.19) meet this requirement, and the results are not sensitive to the factor 10 used in equation (4.19).

At inflow boundaries, all turbulent quantities are specified, while at outflow boundaries, a zero gradient is applied.

Two of the computed flow fields involve rotational symmetry. In these cases, the gradients of all turbulent quantities in the circumferential direction are set to zero.

4.3 Computational grid

For numerical simulations of open-field aerodynamics, two different types of meshes are often adopted: structured and unstructured. Both types allow obtaining adequate results, however, they present both positive and negative aspects that make them more or less suitable depending on the case under study. Unstructured meshes are preferable when it is desired to vary the resolution in the same region efficiently and reduce the number of elements, as well as when it is necessary to discretize complex geometries without significantly increasing the computational cost. On the other hand, structured meshes are executed massively and in parallel, which makes them faster and requires less computational cost. Moreover, structured meshes can be aligned with the flow direction, thus reducing numerical dissipation. The software STAR CCM+ offers two meshing options: an unstructured polyhedral mesh and a structured refined cell mesh.

The construction of the computational grid is based on two cardinal points. The first was to obtain a good approximation of the geometry using surface and volume controls. The second was to achieve a consecutive height of the first cell from the wall. The simplified Prandtl theory for flat plates in the case of turbulent flow was used for the first cell near the wall as explained in the paragraph below.

4.3.1 Y+ Wall Distance Estimation

When meshing a computational domain, it is critical to estimate the appropriate wall-normal distance required to achieve a desired value of y^+. The parameter y^+ is a dimensionless wall distance that characterizes the near-wall region of a turbulent boundary layer and is defined as:

$$y^+ = \frac{\rho u_\tau y}{\mu} \tag{4.20}$$

where:

- ρ is the fluid density,

- u_τ is the friction velocity,

- y is the normal distance from the wall, and

- μ is the dynamic viscosity of the fluid.

The value of y^+ is essential for selecting the appropriate turbulence model and wall treatment in a computational fluid dynamics simulation. For instance, wall-functions are typically used when $y^+ > 30$, while low-Reynolds number models (which directly resolve the viscous sublayer) require $y^+ \ll 1$. Estimating the

wall-normal distance for the desired y^+ value is crucial for grid refinement and accuracy near the walls.

To estimate the wall distance y corresponding to a given y^+, the following steps can be followed:

1. Compute the Reynolds Number:

   The Reynolds number (Re_L) is a dimensionless quantity that compares inertial forces to viscous forces in a fluid flow. It is defined as:

   $$Re_L = \frac{\rho U_\infty L}{\mu} \tag{4.21}$$

   where:

   - U_∞ is the free-stream velocity (velocity far from the wall),
   - L is a characteristic length scale, such as the boundary layer thickness or the length of an object.

   The Reynolds number gives an indication of the flow regime. In turbulent flow, Re_L is typically high (greater than 10^5), and it influences the size of the boundary layer and the nature of the turbulence.

2. Estimate the Skin Friction Coefficient:

   The skin friction coefficient (C_f) relates the wall shear stress to the dynamic pressure of the flow. It is crucial in determining the friction velocity. The skin friction can be estimated using empirical correlations such as Schlichting's correlation for turbulent boundary layers over a flat plate:

   $$C_f = [2\log(Re_x) - 0.65]^{-2.3} \tag{4.22}$$

   This formula is valid for turbulent boundary layers in external flows over smooth surfaces.

3. Compute the Wall Shear Stress:

   The wall shear stress (τ_w) is a measure of the force exerted by the fluid on the surface due to viscous effects. It is calculated as:

   $$\tau_w = \frac{1}{2}\rho U_\infty^2 C_f \tag{4.23}$$

   The term $\frac{1}{2}\rho U_\infty^2$ is the dynamic pressure of the flow, and C_f represents the fraction of this dynamic pressure that contributes to the shear stress on the wall.

4. Compute the Friction Velocity:

The friction velocity (u_τ) is a velocity scale related to the wall shear stress and is used to non-dimensionalize the wall distance. It is given by:

$$u_\tau = \sqrt{\frac{\tau_w}{\rho}} \tag{4.24}$$

The friction velocity is a key parameter in determining y^+ and represents the velocity at the wall that governs the structure of the near-wall flow. Higher wall shear stress results in higher friction velocity, which leads to a larger y^+ for the same physical wall distance.

5. Compute the Wall Distance:

Finally, the wall distance y corresponding to a target y^+ value can be calculated by rearranging Equation (4.20) as follows:

$$y = \frac{\mu y^+}{\rho u_\tau} \tag{4.25}$$

This equation is used to determine the normal distance from the wall required to achieve a specified y^+ value. The suitable value desired to resolve the viscous sublayer is $y^+ = 1$. It is considered to be the upper limit for accurate resolution of the viscous sublayer.

Chapter 5

Computational domain

5.1 Case study

5.1.1 Geometry

The Vertical Axis Wind Turbine taken into exam for this thesis' work was built by Yosry et al. [31] and tested in a wind tunnel. The VAWT is the straight bladed type with end plates, which mitigate the tip vortex production and increase the overall efficiency. A review was conducted by the authors to find the best parameters, the characteristics of the turbine are resumed in the table below:

Parameter	Value
Rotor diameter (D)	0.15 m
Rotor height (H)	0.15 m
Blade profile	NACA-0015
Chord length (C)	0.05 m
Solidity (σ)	1
Number of blades (n)	3
Shaft diameter (d_s)	0.01 m

Table 5.1: VAWT geometrical parameters

The height-diameter ratio is set to 1 as it has been found to obtain better overall performances [32]. The blade profile of choice is the NACA-0015, which has shown great performances in low wind conditions [33]. Having a chord value of 0.05m, brought a solidity value of 1. High values of solidity are associated with better low wind performances and higher power coefficients. Low solidity values on the other hand are associated with better performances at high tip speed ratio [34]. The turbine rotor has been installed outside the tunnel section without any blockage or

wall restrictions. The wide domain allows focusing on the flow phenomena around and inside the high solidity rotor, and confirms the open-field operating conditions.
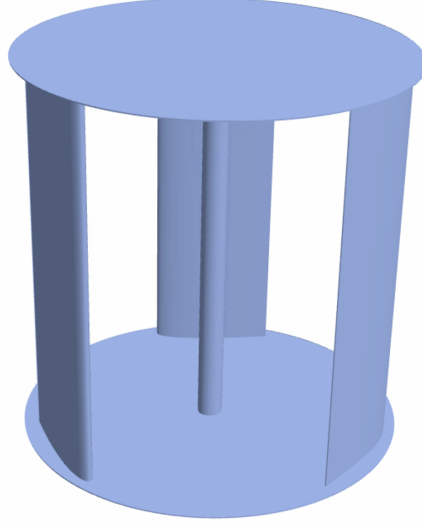

Figure 5.1: 3D model of the VAWT

5.1.2   Experimental Setup

The authors carried out experimental tests in an open-circuit subsonic wind tunnel. The wind is discharged through a 30 kW axial fan, which is controlled by a variable frequency driver, reaching a maximum wind speed of 36 m/s. In order to obtain a steady turbulence flow, the wind crossed a honeycomb net to the settling chamber after the diffuser section, and is finally discharged from a nozzle with a 1:12 area ratio and a 0.75×0.75 m^2 test section. The blockage ratio (defined as the turbine area to the tunnel cross-sectional area) for the current experiments is about 4%. However, the blockage effects are insignificant as the turbine has been tested in the outer part of the wind tunnel, far enough away from the nozzle discharge to avoid any wall restrictions. The turbulence intensity is about 0.7%, measured for an averaged integral length scale of 0.1 m.

The wind tunnel is equipped with a Pitot tube, differential, and digital manometers to characterize the wind flow at different sections. The rotor is supported using a portable aluminium structure, allowing the turbine to be centered in front of the test section at a distance equal to 6 times the turbine diameter. The rotational axis is supported, above and below, by two radial bearings. The brake-torque measuring system is placed at the top of the aluminium structure and is connected to the turbine mechanically through two flexible couplings. The measuring system

includes a high-precision torque and rotational speed sensor, governed by a control and data acquisition setup. It is combined with a hysteresis brake, with a precision of 0.1% in the torque and 0.015% in the rotational speed.
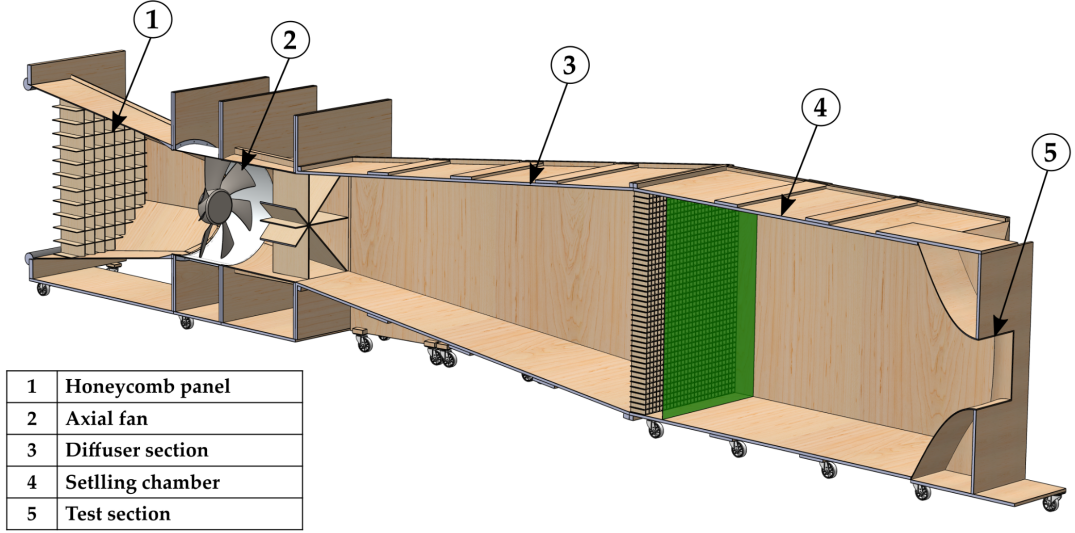

1	Honeycomb panel
2	Axial fan
3	Diffuser section
4	Setlling chamber
5	Test section

Figure 5.2: Wind tunnel setup

Experimental runs have been carried out for different wind velocities: 7.0 m/s, 8.0 m/s, 9.0 m/s, and 10.0 m/s. For each velocity, the turbine rotates freely without any loading until reaching the steady-state condition where the rotational speed is nearly constant. Thereafter, the turbine is gradually loaded by changing the input current to the brake. Subsequently, the rotational speed decreases, and the torque produced rises until reaching the maximum power point. From that point onwards, the power output from the turbine decreases with the decline of the rotational speed until the turbine reaches an unstable condition and stops.

For each test, the rotational speed (ω), the wind velocity (U_∞), and the mechanical torque (T) are measured. These registered parameters are post-processed to calculate the power output (P) and the dimensionless parameters: the power coefficient

$$C_p = \frac{P}{0.5 \cdot \rho \cdot A \cdot U_\infty^3} \tag{5.1}$$

and the tip speed ratio

$$\lambda = \frac{\omega \cdot R}{U_\infty} \tag{5.2}$$

36

5.2   2D Numerical methodology

Two-dimensional CFD simulations offer several advantages in the study of Vertical Axis Wind Turbines, particularly during the early stages of design and analysis. While these simulations do not fully capture the complexities of three-dimensional flow, they provide valuable preliminary insights while significantly reducing computational costs and simulation time.

One of the primary benefits of using 2D simulations is the ability to analyze the flow behavior around key components of the turbine, such as the airfoil shapes of the blades. In the case of VAWTs, the flow around the blades varies substantially during each rotation cycle, and 2D simulations can help identify important phenomena such as flow separation, vortex formation and shedding, and pressure distribution along the blades. These insights are crucial for better understanding the aerodynamics of the system, even though more complex three-dimensional effects, like turbulence or vertical flow variations, are not resolved.

Another advantage of the 2D approach is the opportunity to optimize the computational mesh and simulation parameters. By working with a simplified model, it is possible to test different meshing strategies, turbulence models, and boundary conditions more quickly and cost-effectively. For VAWTs, this optimization phase is critical because the complex geometry and rotational motion of the blades require careful resolution of the flow field. Conducting this initial phase in 2D allows potential issues to be identified and resolved, ensuring that when transitioning to 3D simulations, the model is already well-configured, reducing the risk of errors or inefficiencies.

2D simulations are also particularly useful for conducting feasibility studies during the preliminary stages of VAWT design. Before committing to more resource-intensive 3D simulations, 2D simulations provide a fast and efficient way to assess whether a particular blade configuration or turbine design is promising. For instance, if a certain blade geometry performs poorly in a 2D simulation, it is unlikely to perform well in a more complex three-dimensional setup. This early identification of potential design failures saves both time and resources.

Lastly, while three-dimensional simulations are necessary for a complete understanding of the aerodynamics of VAWTs—especially for phenomena such as three-dimensional turbulence, vertical scale effects, and blade interactions—2D simulations serve as an effective preliminary step. They help gain foundational insights, reduce the likelihood of setup errors in 3D simulations, and refine the design before moving on to more complex and computationally expensive studies.

5.2.1 Computational Domain and Overset Grid

The computational domain for the two-dimensional CFD simulation of a vertical-axis wind turbine (VAWT) is designed to replicate a wind tunnel environment with appropriate boundary conditions to simulate free-stream flow. The domain at this stage is set up in order to prevent the influence of boundary conditions on the flow around the turbine. The domain is rectangular, with dimensions of $100D \times 180D$, where D is the diameter of the turbine rotor. This also allows the wake to develop fully, ensuring a more accurate simulation of the aerodynamic behavior of the turbine. Moreover, the pressure bubbles that are formed near the turbine are allowed to develop freely, avoiding numerical errors due to their interaction with the domain walls. The validation simulations will obviously fully represent the experimental setup described in the case study.

Within this domain, a rotating overset grid is implemented to handle the movement of the turbine blades [Fig. 5.3]. The overset region is a circular sub-domain of radius 20 cm ($2.66D$), which moves with the rotor as it spins. The dimension of the rotating domain is chosen accordingly to other studies [18, 19]. This region encloses the rotor and a portion of the surrounding flow, enabling the accurate simulation of blade motion and the complex unsteady aerodynamic interactions [20]. The rotating region must be larger than the VAWT diameter to avoid discontinuities at the interface with the static region. However, since the rotating region is one of the most cell-dense areas, making it too large would significantly increase computational time, reducing the overall efficiency of the simulation. The overset grid is embedded into the static background grid, and its position is updated at each timestep to follow the rotation of the turbine.

This larger overset region provides several important benefits:

- Wake capturing: The wake generated by the turbine blades influences the flow field beyond the rotor's immediate vicinity. A larger overset region ensures that the near-wake effects, including flow separation and vortex formation, are captured with sufficient resolution.

- Smoother grid transitions: By making the overset region larger than the rotor, smoother transitions between the moving and stationary grids are achieved. This helps minimize numerical errors at the grid interfaces, where interpolation between the moving overset grid and the static background grid occurs.

- Numerical stability: A small overset region could lead to abrupt changes in grid resolution and grid quality near the turbine blades, which might introduce numerical instabilities. The larger overset region ensures a more gradual change in mesh size and higher-quality interpolation, leading to improved numerical stability. Particular attention must be paid to the timestep choice,

it is crucial to evaluate it correctly in order to avoid divergence. This topic will be discussed later on.

The use of an overset grid in this simulation allows the rotor to rotate without requiring the entire domain to be rotated, which significantly reduces computational cost. By localizing the high-resolution mesh around the blades and coupling it with the coarser background grid, the simulation can resolve the key aerodynamic phenomena associated with the turbine blades' rotation while keeping the computational effort manageable. It is also crucial to ensure that the cell sizes at the interface between the two regions are compatible. A significant mismatch can lead to large computational errors, potentially nullifying the efforts invested in creating an accurate mesh.
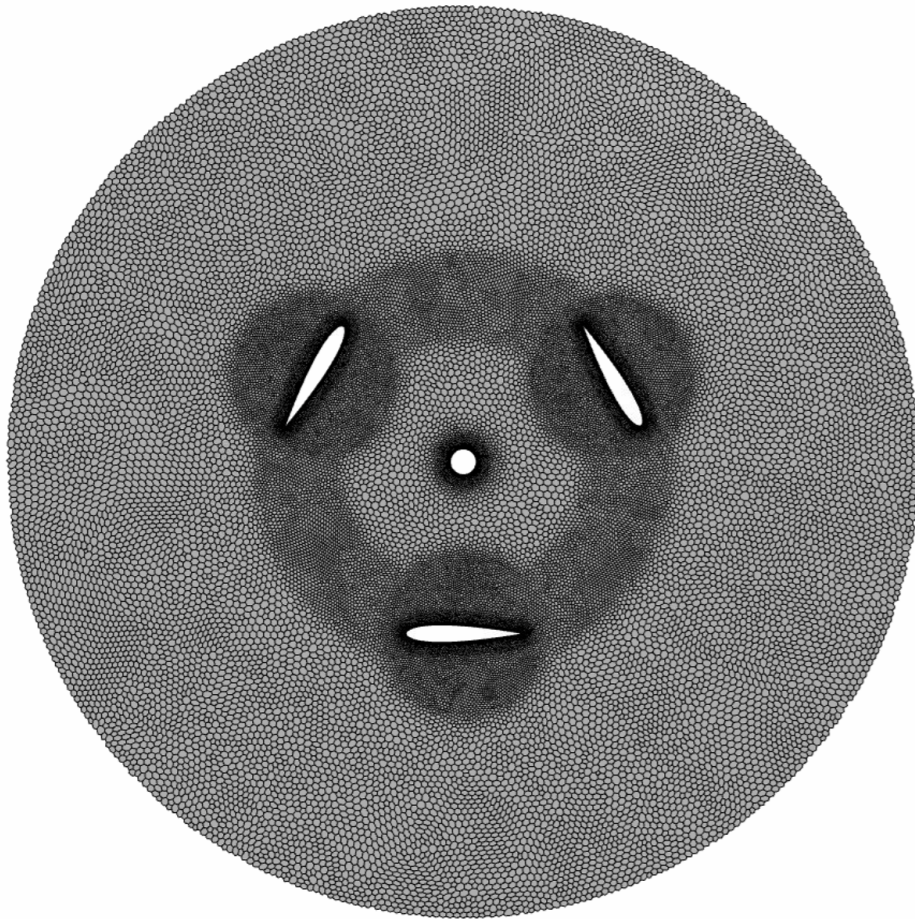

Figure 5.3: The overset region mesh

Domain region

- **External domain region:** This region includes part of the domain where the changes during the simulation are minimal, therefore the target size is set to 1000% of the base size as it would result a waste of resources to make it finer.

- **Wake region:** The downstream region of the VAWT has been divided into seven cone-shaped zones, each progressively less refined as the distance from the turbine increases. This passage is necessary to fully capture the wake development. The zone closest to the turbine shares the same mesh specifications as the rotating region to ensure mesh consistency and minimize computational errors caused by the interface. The subsequent zones utilize mesh sizes of 40%, 60%, 90%, 110%, 150%, 200% and 300% of the base size, respectively, and extend over distances of 0.25, 0.5, 1, 3, 5, 7 and 11 meters. This approach, combined with the conical shape of the zones, ensures accurate capture of the wake evolution [Fig. 5.4].
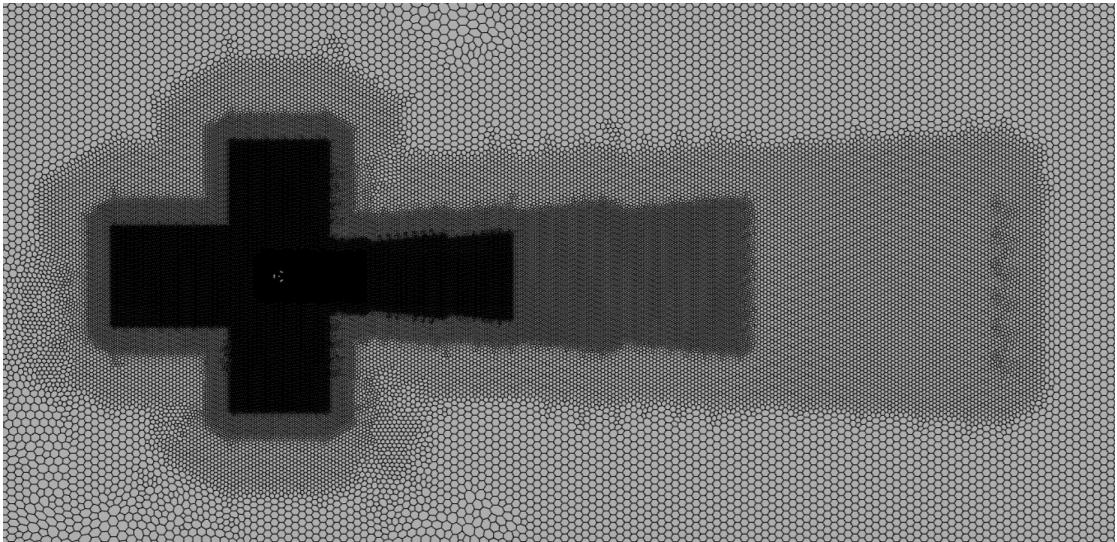

Figure 5.4: Domain region

- **Bubble region:** During the mesh setup, the formation of pressure bubbles was observed on both sides of the turbine and in the area immediately upstream. These structures can significantly influence the results, so accurately capturing them is essential. To address this, two box-shaped refinement regions were placed around the bubbles. The mesh density within these regions was chosen to capture the phenomenon with sufficient detail, while keeping the computational cost manageable [Fig. 5.5].
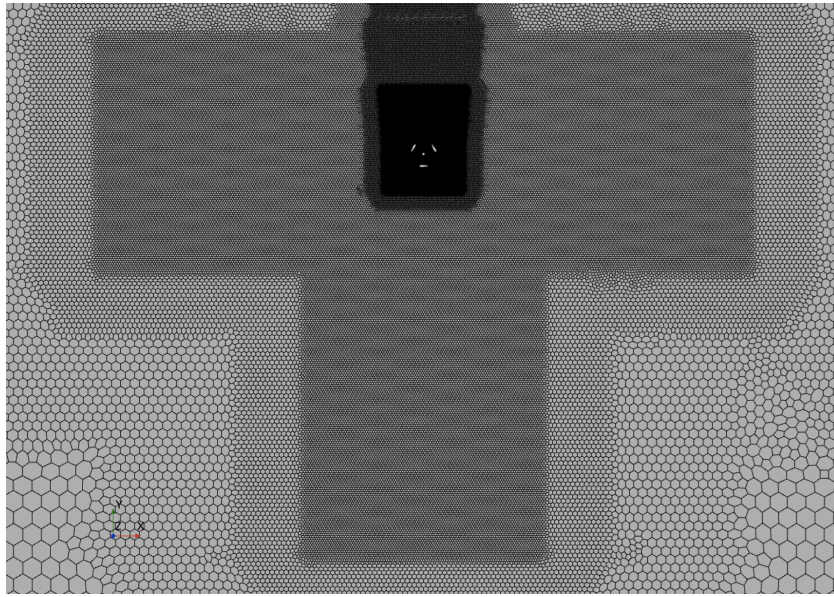
Figure 5.5: Bubble region

Overset region

The overset region contains the turbine model, so it must be the most cell-dense region of the whole domain. The maximum size set for the rotating region is 20% of the base size.

The blades' surfaces and surrounding area need a more detailed analysis. The meshing process for this CFD simulation is fundamentally dependent on the quality of the CAD model used. If the spatial discretization of the points defining the blade profile is insufficient, the resulting geometry may exhibit sharp angles instead of smooth curves. This can lead to inaccurate predictions of flow behavior, such as premature stall or flow separation in the wrong locations, which do not reflect the actual aerodynamic performance of the turbine [35]. To address this issue, a cosine distribution of 500 points per blade profile was applied. This distribution allows for a higher concentration of points near the leading and trailing edges, where the curvature is more pronounced, ensuring a more accurate representation of the geometry and eliminating the risk of sharp angles.

Several key factors were taken into consideration when setting the mesh parameters around the VAWT blades. Since the blades are the most critical part of the turbine, it is essential to ensure that the mesh is fine enough to capture the complex flow phenomena occurring in their vicinity. As discussed in Chapter 2, the blades experience dynamic stall during each rotation cycle, making it crucial to accurately model the near-blade region. This ensures that the complex aerodynamic behavior,

including flow separation and vortex shedding, is captured correctly.

In particular, special attention was given to refining the boundary layer near the blades to accurately capture the flow characteristics and stall behavior. Additionally, a curvature-based refinement strategy was adopted to ensure a finer mesh in regions with high curvature, such as the leading and trailing edges. This approach guarantees that the blade geometry is represented smoothly and avoids potential numerical errors associated with poor mesh quality. Furthermore, careful consideration was given to the resolution of the wake behind the blades, as it plays a significant role in the turbine's overall aerodynamic performance. Finally, the quality of the overset grid, which allows the blades to rotate, was optimized to ensure smooth transitions and minimize interpolation errors.

By taking all of these factors into account, the mesh was designed to ensure that the simulation captures the complex, unsteady aerodynamic phenomena associated with the VAWT blades, leading to a more accurate representation of the turbine's performance.

The following list outlines the key parameters used for the mesh:

1. **Blade surface:** The target cell size on the blade surface is set to 4% of the base size, with a minimum surface size of 0.5%. This configuration, combined with a surface curvature setting of 120 points, ensures a fine discretization of the mesh, particularly at the leading edge, where dynamic stall is expected to initiate [Fig. 5.6a].

2. **Trailing edge:** Two surface controls are applied to the trailing edge. First, the mesh is further refined with a target size of 0.4% of the base size. To capture the flow behavior more accurately in this critical region, the surface growth rate is reduced from the standard value of 1.2 to 1.1. The second modification involves the removal of the prism layer, as the flow separation occurring in this area is not well captured by this type of mesh structure [Fig. 5.6b].

3. **Prism layer region:** The configuration of the prism layer is essential for obtaining reliable results. The total thickness of the prism layer is set to $0.001m$, with the first layer thickness calculated using the method described in Chapter 3. For stability during the convergence process, as will be discussed later, the chosen value for this parameter is $1.0 \times 10^{-5}m$. Additionally, the number of prism layers is critical to maintain the correct mesh shape, and for this reason, 29 layers were applied [Fig. 5.6c]. The same configuration is also applied to the central rod located on the axis of the VAWT [Fig. 5.6d].

4. **Near blade region:** The mesh refinement in the near-blade region is carried out in two stages, both aimed at capturing the shedding and evolution of

vortices created by the stall process. The first volumetric control is applied to a region offset from the blade profile and has a target size of 5% of the base size. The second volumetric control uses a cylindrical region with a diameter of $1.2c$ (where c is the chord length) and a target size of 8% of the base size.

5. **Blades' wake:** The wake region is modeled as a hollow cylinder enclosing the three blades. The target cell size in this region is set to 10% of the base size, ensuring sufficient resolution to capture the wake dynamics.

It is important to note that all mesh customizations, except for the prism layer thickness, are defined relative to the base size. This approach ensures consistency and reliability during the mesh convergence process, as it allows any observed behavior to be directly linked to the cell size, facilitating the identification of its underlying cause.
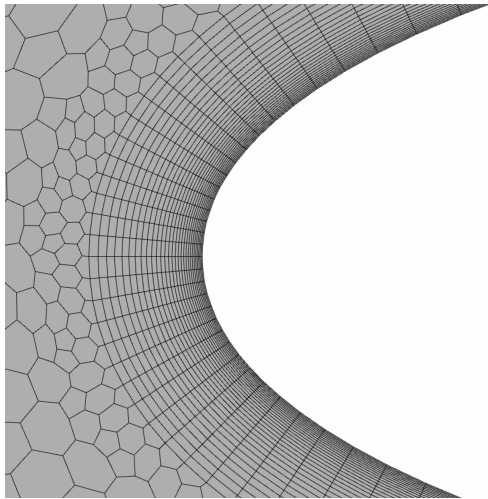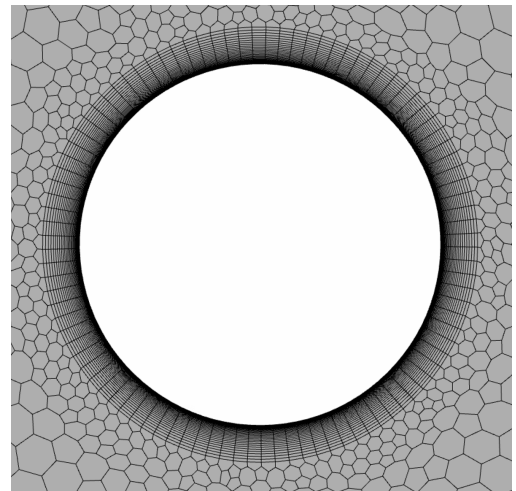
(a) Leading edge
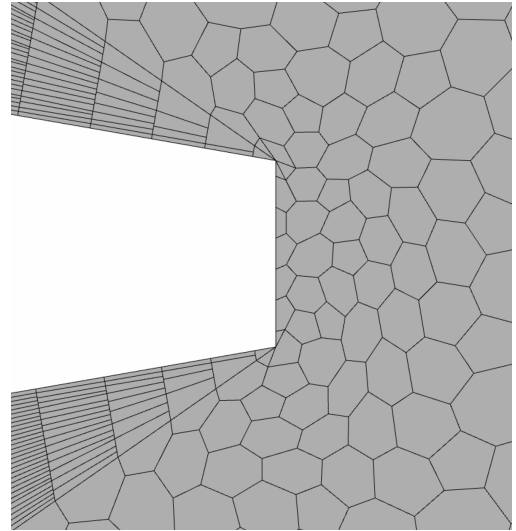
(b) Trailing edge
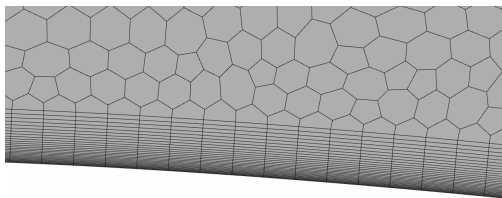
(c) Prism layer

(d) Central shaft

Figure 5.6: Mesh refinements

5.3   Fluid flow and Turbulence Modeling

The fluid being simulated is a gas, assumed to have a *constant density* set to $1.18415 kg/m^3$, as the flow velocities are very low.

The solver used in this simulation is the *Implicit Unsteady*, designed for time-dependent flows. This method offers greater numerical stability, allowing for larger time steps without compromising accuracy, which is especially important in flows with transient behavior. The simulation adopts an *All y+ Wall Treatment* for modeling the boundary layer, ensuring robustness across a wide range of near-wall grid resolutions. This approach accurately handles both low and high y^+ values, making it suitable for simulations with varying mesh refinement near the walls. Additionally, the inclusion of a *Realizability Coefficient* ensures that turbulent quantities like kinetic energy remain physically meaningful, preventing unrealistic or non-physical results. The standard $\gamma - Re_\theta$ transition model was implemented to simulate the transition from laminar to turbulent state. This model is particularly useful in predicting separation points in flow fields, especially in cases where fully turbulent flow might not yet have developed.

For the numerical solution, a *Segregated Flow* approach is used, where the velocity and pressure fields are solved independently. Although computationally less intensive than coupled solvers, this method requires additional iterations to achieve proper convergence. In this case, the SIMPLE algorithm is used to handle the pressure-velocity coupling. A second-order convection scheme is applied to the discretization of the convective terms in each RANS equation, with the main advantage being improved accuracy in convection-dominated flows, especially in scenarios involving sharp gradients, flow separation, or complex boundary layers. *Solution Interpolation* is employed to ensure that flow variables are accurately interpolated between mesh cells, maintaining stability and precision in regions of the flow with rapidly changing gradients or a coarse mesh.

The simulation is two-dimensional at this stage, meaning that the flow is solved in two spatial dimensions, typically assuming no variation in the third dimension. While this simplifies the problem and reduces computational cost, it may limit the ability to capture fully three-dimensional flow structures. Lastly, the *Wall Distance* was calculated using an "implicit tree" method, which efficiently computes the distance from a point in the flow field to the nearest wall. Accurate wall distance calculations are crucial for turbulence models, which rely on near-wall information to compute quantities such as turbulence dissipation and viscosity near solid boundaries.

The simulation follows a *Reynolds-Averaged Navier-Stokes* (RANS) methodology, in which the Navier-Stokes equations are averaged to separate the mean flow from turbulent fluctuations, thus reducing computational complexity while effectively modeling turbulence effects. The turbulence model chosen for the simulation is the

SST k-ω model developed by Menter, as anticipated in Chapter 4. The coefficients listed in Chapter 4 remain unchanged from the standard values, as they provided the most accurate results, apart from the *Curvature Correction Parameters*, which were applied to account for the effects of streamline curvature on turbulence production. This correction is crucial in flows involving swirling or rotational effects, as is the case here. The last correction is made to the turbulence length scale which is set to 4% of the prism layer thickness. The turbulence length scale represents the size of the largest eddies in a turbulent flow and indicates the spatial extent over which turbulence energy is generated before cascading to smaller scales. In URANS simulations, the length scale plays a critical role in determining the behavior and dynamics of turbulent flows over time. Correct specification of the length scale allows the model to accurately compute how energy is transferred between vortices and how turbulence interacts with unsteady phenomena, such as vortex shedding or flow separation.

5.3.1 Boundary and initial conditions

Boundary conditions are applied to the inlet, outlet, and walls of the domain. As is common in CFD simulations [18, 19, 36] of Vertical Axis Wind Turbines (VAWTs), a velocity inlet and a pressure outlet are defined in the direction of the freestream wind, the lateral boundaries are treated as pressure outlets too with the atmosferic pressure as reference. The turbine surfaces are modeled as no-slip walls, as required for accurate representation of the flow around solid surfaces.

The freestream wind speed (U_∞) is set as an initial condition and remains constant throughout each simulation, varying between $7\,\mathrm{m/s}$ and $10\,\mathrm{m/s}$ to replicate the conditions of the experimental setup. While in a physical experiment the turbine would rotate in response to the wind, in the simulation the rotational speed is prescribed and held constant. To evaluate performance at different tip-speed ratios (TSR), the rotational speed is varied from a minimum of $800\,\mathrm{rpm}$ to a maximum of $1700\,\mathrm{rpm}$.

5.4 Computational setup

5.4.1 Grid convergence

Before conducting the grid convergence study, an analysis was performed to determine the number of revolutions necessary to ensure result convergence. The simulation used for the following tests is performed at $U_\infty = 10m/s$ and rotational speed of $1000rpm$. The most frequently used convergence criterion is the one that requires the variation of the moment coefficient to be below 1% for two consecutive revolutions. This criterion allowed the identification of the minimum number of

revolutions required to obtain reliable results, which was found to be 7. This value is in line with other studies results [28, 18].

In addition to this initial test, a second test was carried out to assess whether averaging over different numbers of revolutions after convergence significantly affected the results. This step is essential for establishing in advance how many revolutions the turbine must complete to reduce simulation time while still obtaining accurate results. For this test, a 30 revolutions simulation was performed and the torque mean was calculated over the last 1, 3, 5, 8, 10 and 12 rounds. The difference in torque mean found between the 5 and 12 rounds tests is below 1% as shown in Fig. 5.7, so the 5 rounds mean was chosen.
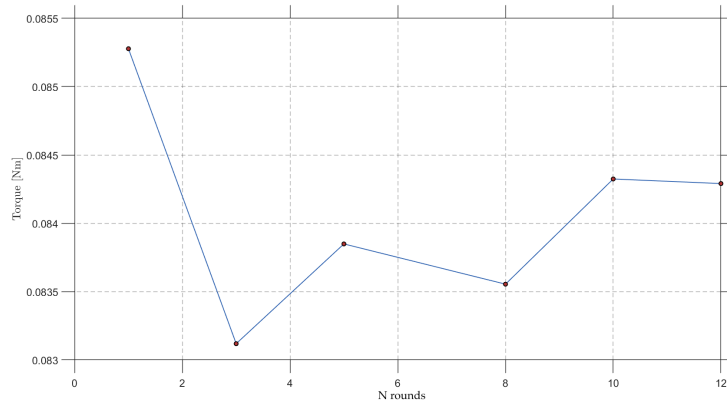

Figure 5.7: Torque mean over different number of rounds

Grid convergence is a crucial aspect of validating the accuracy of a numerical simulation. In this context, grid convergence refers to the process of refining the computational mesh and ensuring that the key flow quantities, such as torque, become independent of the grid resolution. A series of simulations are performed using successively finer grids, and the results are compared to verify that the solution approaches a stable value. This ensures that the numerical error due to discretization is minimized. The choice of an adequately refined grid not only ensures the accuracy of the simulation but also helps reduce computational cost by avoiding unnecessary over-refinement. Once grid convergence is achieved, the results can be considered reliable for further analysis. For the evaluation of the mesh convergence, the Eça and Hoekstra method was used [37]. This method provides a systematic approach to assess the numerical accuracy of CFD simulations by focusing on the estimation of the discretization error. It involves calculating the observed order of convergence (p), which represents how the error decreases with mesh refinement, and comparing it with the theoretical order expected from the numerical scheme. To estimate the error, simulations are performed on a series of progressively finer grids, and the change in results is analyzed. The method

47

also introduces a safety factor to account for uncertainties in the discretization error estimation. This approach is an enhancement of the Grid Convergence Index (GCI) method by Roache, offering a more accurate and reliable means to quantify numerical errors and ensure proper convergence behavior. The refinement process helps verify that the solution approaches the exact result as the grid becomes finer, ensuring confidence in the simulation's predictive capability.

During the grid refinement process, several factors must be carefully considered to ensure consistency and reliability in the simulation results. First and foremost, the base size of the mesh must be scaled by a constant factor, so that the grid remains consistent across different refinement levels. The overall mesh topology should remain unchanged, except for the variation in base size. To achieve this, every surface or volume that contains a custom mesh has been directly correlated to the base size and scaled accordingly, as described in the previous sections. The only exception to this rule is the prism layer. The prism layer maintains a constant thickness independent of the base size, but the number of prism layers increases linearly as the base size decreases. This approach is adopted to preserve the elongated quadrilateral shape of the cells within the prism layer. This specific cell geometry is essential for accurately capturing the complex phenomena within the boundary layer, particularly the flow separation that occurs during the stall phase of the VAWT blades.

The base size has been varied from a maximum of 0.04 meters to a minimum of approximately 0.01 meters through 7 iterations, using a scaling factor of 1.25 between consecutive mesh levels. Correspondingly, the number of layers in the prism region has been adjusted from a minimum of 15 to a maximum of 40 layers. This refinement strategy ensures that the boundary layer near the turbine blades is adequately resolved, which is critical for capturing the near-wall flow features and improving the accuracy of the aerodynamic forces computed during the simulation. Moreover, maintaining the quadrilateral structure of the prism cells allows for a more stable representation of the viscous sublayer, which plays a significant role in accurately modeling the transition and separation phenomena that occur during turbine operation, particularly in the high-angle-of-attack regimes associated with stall.

As observed in other studies [18, 21], the quantity chosen for performing the grid convergence analysis is the average torque. Specifically, the average torque over the last 5 revolutions of the turbine was considered as explained above.

This decision is driven by the observation that the flow field, after an initial transient phase, reaches a quasi-periodic state. In this state, the torque fluctuations between successive revolutions tend to stabilize, allowing the use of fewer revolutions to compute the average without losing accuracy. Reducing the number of revolutions used for averaging helps optimize the computational cost, especially in grid convergence studies, where multiple simulations at different grid resolutions

are required. By ensuring that the torque has reached a stable periodic behavior, the results remain reliable even when the number of revolutions used for averaging is minimized. This approach balances computational efficiency with the need for accuracy in capturing the dynamic behavior of the turbine. With all these considerations in mind, the chosen approach was split in two phases: an initial transient phase characterized by a larger timestep where the wake can develop, followed by a second phase with a smaller timestep where all the torque data is collected.

5.4.2   Timestep

The selection of an appropriate timestep is another critical factor in simulations. A timestep that is too large can result in poor resolution of the transient flow phenomena, such as vortex shedding and dynamic stall, leading to inaccuracies in the prediction of aerodynamic forces like lift and drag and consequently torque. On the other hand, a timestep that is too small may significantly increase the computational cost without offering substantial improvements in accuracy. For a VAWT, which operates under unsteady and highly dynamic conditions, capturing the correct interaction between the blades and the flow is essential. The turbine blades experience rapidly changing angles of attack as they rotate, which can lead to complex flow patterns, including separation and reattachment. To accurately resolve these phenomena, the timestep must be chosen such that the rotational motion of the blades is well-resolved while ensuring numerical stability. Typically, the Courant-Friedrichs-Lewy (CFL) condition is used as a guideline to select the timestep. This a criterion used to ensure the numerical stability of time-dependent simulations. It defines the maximum allowable timestep Δt in relation to the grid size Δx and the velocity of the flow u, ensuring that information does not travel across more than one grid cell in a single timestep. The CFL number is typically defined as:

$$CFL = \frac{u\Delta t}{\Delta x} \tag{5.3}$$

Where u is the stream velocity, Δt is the timestep and Δx is the minimum cell size. For explicit methods, it must remain less than or equal to 1 for stability. In implicit methods, like in this case, larger timesteps are allowed, often resulting in CFL numbers much greater than 1, since these methods are more stable and can handle larger time increments without violating the stability condition. It is really important to check the behavior of the simulation to evaluate the correct definition of the parameters. In this case a value of $CFL = 13.33$ was estimated, which can be considered acceptable. No divergence of solution or artifacts were noted during all the simulation process.

Chapter 6

Results validation and discussion

Numerous studies, including the case study presented in this work, employ a variety of graphs to represent the performance of vertical axis wind turbines (VAWTs). The most common metrics used are the power coefficient (C_p) plotted against different values of the tip speed ratio (λ), and the turbine power output (P) as a function of the operational range of rotational speeds (expressed in rpm). These two representations are closely related, as explained in the previous sections, where the C_p-λ relationship directly influences the power output curve.

However, in the case study, a significant discrepancy was observed: the experimental P-rpm curve does not correlate with the corresponding C_p-λ values, as one would expect based on the theoretical relationships. This mismatch suggests that either the experimental setup introduced additional variables or the data was not processed consistently, leading to inaccurate representation of the turbine's performances across these two critical metrics. A more thorough analysis is required to fully understand this inconsistency and ensure the results accurately reflect the turbine's behavior.

Taking into account the error found within the case study, the reliability of the study is undermined. Despite this, the results obtained have been compared with those presented, and only the most reliable data have been retained, specifically the C_p-λ curves. An additional representation discrepancy was noted: in two graphs representing the same C_p-λ curve for a wind speed of 10 m/s, the values deviate by approximately 10%.

In light of this, the values reported in the study should be taken with caution, and the comparison should be considered qualitative rather than quantitative. The presence of more accurate results would undoubtedly improve the evaluation and discussion of the outcomes presented in this thesis. Nevertheless, the results were

compared with the most reliable data, and the conclusions drawn remain largely independent of the data extracted from the case study.

This chapter serves another purpose, to show directly the unreliable results obtained from the application of the k-ε turbulence model.

Before showing the results of the simulations, a choice for the parameters of base size and timestep has still to be made.

6.1   Convergence study results

The convergence study is performed as explained in Chapter 5 and the results are displayed below:
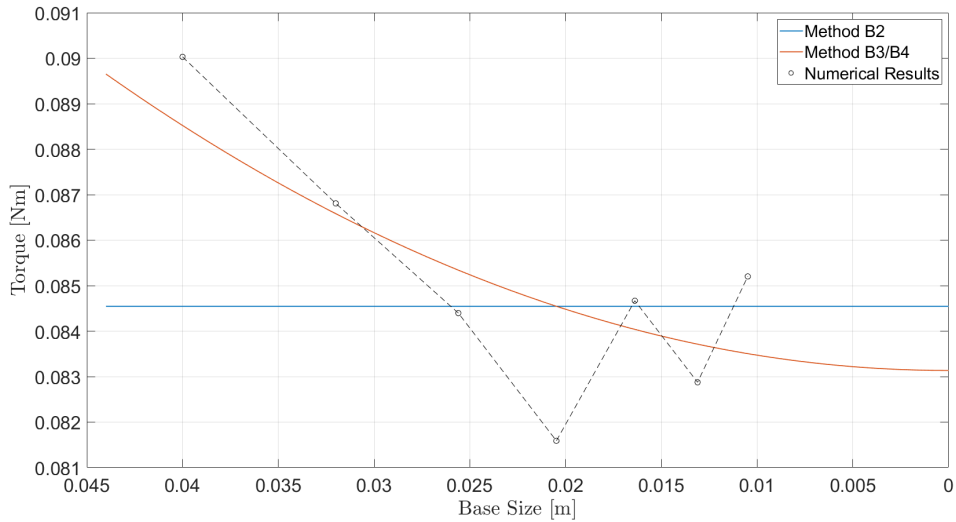
Figure 6.1: Convergence study on the average torque

In Fig. 6.1, three lines are present: the blue line represents the variation in torque values calculated using the B2 method, the red line uses the B3/B4 method, while the dashed black line indicates the trend of results obtained from CFD analyses. It can be noted that the B2 method should be discarded, as it shows total independence from the base size, which makes it unreliable. On the other hand, the trend of the B3/B4 method follows that of the CFD data, indicating a theoretical average torque value of approximately 0.0832 Nm.

In Fig. 6.2, a different visualization approach is employed, where error bars are included to assess the reliability of the results. The significant difference in error between large and small base sizes is evident, further reinforcing the validity and accuracy of the convergence study presented here.
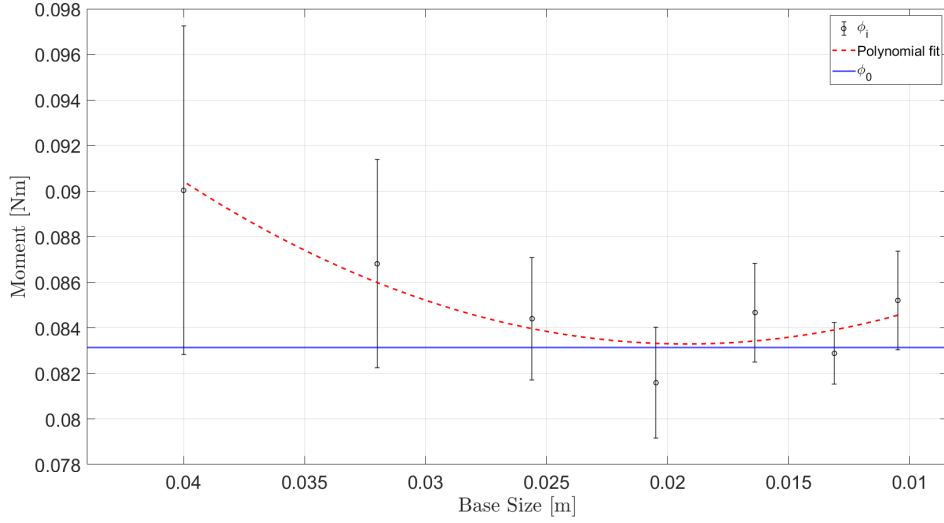
51

Figure 6.2: Convergence study with error bars calculated using Hoekstra's B3/B4 method

Further insights can be drawn from the trend in the computed data. An oscillatory behavior becomes apparent when the base size is reduced below $0.02\,\mathrm{m}$. This phenomenon could be attributed to insufficient temporal discretization, which leads to an excessively high CFL number. It is essential to recall that the CFL number is influenced by both the cell size and the selected timestep. When the timestep is kept constant, reducing the cell size inevitably increases the CFL number. Although no instances of solution divergence were observed, inaccuracies in the calculations remain a possibility.

Additionally, it is important to consider the computational time required for the simulations. In many cases, slightly less accurate results are deemed acceptable if they lead to significantly shorter simulation times. Fig. 6.3 illustrates the relationship between the base size and simulation time, showing an exponential increase in time for base sizes smaller than $0.02\,\mathrm{m}$. This trend suggests that while refining the mesh can improve accuracy, it also results in a dramatic increase in computational cost.

This behavior is further confirmed by the data shown in Fig. 6.4, where the same pattern emerges. In this case, the y-axis represents the total number of cells in the mesh. As the base size decreases, the number of cells rises steeply, leading to a corresponding increase in the simulation time. This exponential growth underscores the need for a tradeoff between accuracy and computational efficiency in convergence studies. Careful selection of the base size is therefore crucial, as excessively fine meshes can lead to diminishing returns in accuracy while

52

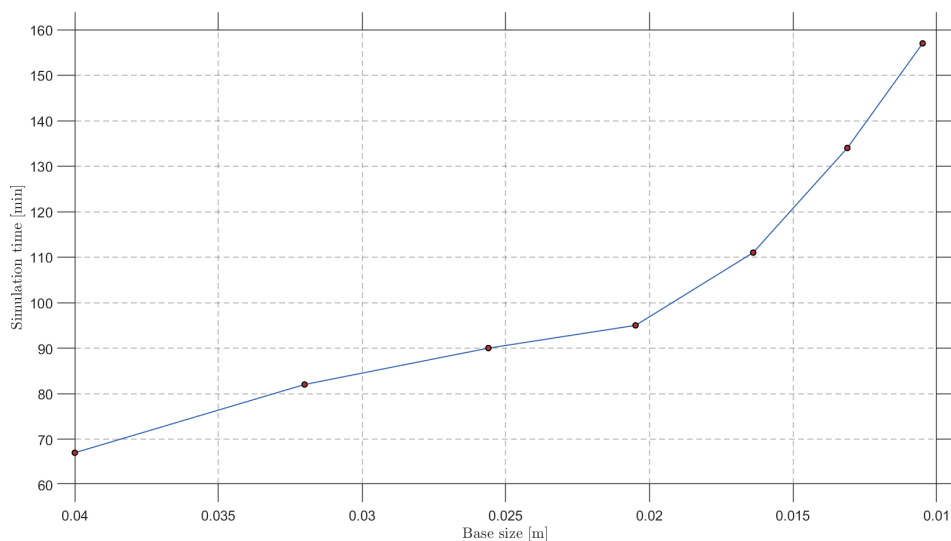disproportionately increasing the time and computational resources required.

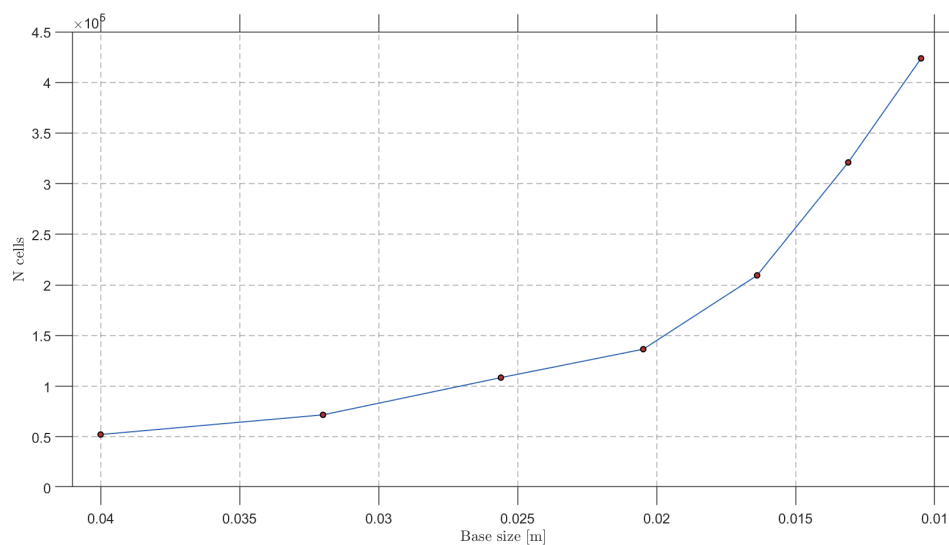**Figure 6.3:** Simulation time at different base sizes

Figure 6.4: Mesh cell count at different base sizes

The last piece of information that was used to choose the base size is the torque's time history.

Greater base sizes fail to accurately represent the creation and evolution of vortices. This can be noticed both in the amplitude and in the cleanliness of
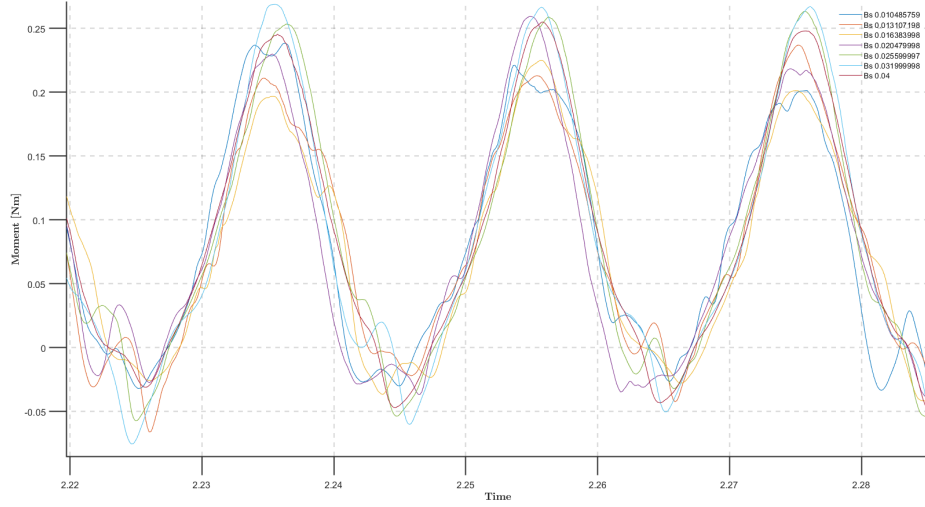
Figure 6.5: Torque's time history

the curves at base sizes closer to 0.04 m. As the base size gets smaller, much more turbulent phenomena can be observed. Lower peaks highlight the increased accuracy in capturing more turbulent behaviors.

Given these observations, a base size of 0.015 m was selected. As is common in convergence studies, a tradeoff between the accuracy of the results and the computational time was made, leading to this decision.

6.2 Timestep study results

The timestep selection plays a critical role in determining the accuracy of the simulation results, especially when dealing with transient fluid dynamics problems such as those involving rotating turbines. As mentioned in the previous chapter, the primary criterion for choosing an appropriate timestep was the CFL number, which ensures numerical stability and accuracy in resolving the flow field.

To investigate the influence of the timestep on the results, a series of simulations were conducted, varying the timestep from 180 to 720 iterations per turbine revolution following other studies configuration [18, 24, 26, 38]. This corresponds to an angular step ranging from 2° to 0.5°. The primary objective of this test was to evaluate the effect of time discretization on the average torque output. The results, illustrated in Fig. 6.6, clearly show the impact of timestep selection on the computed torque values.

It is worth noting that while the difference in average torque between the 0.5° and 0.8° discretizations is relatively small, around 1%, the computational time
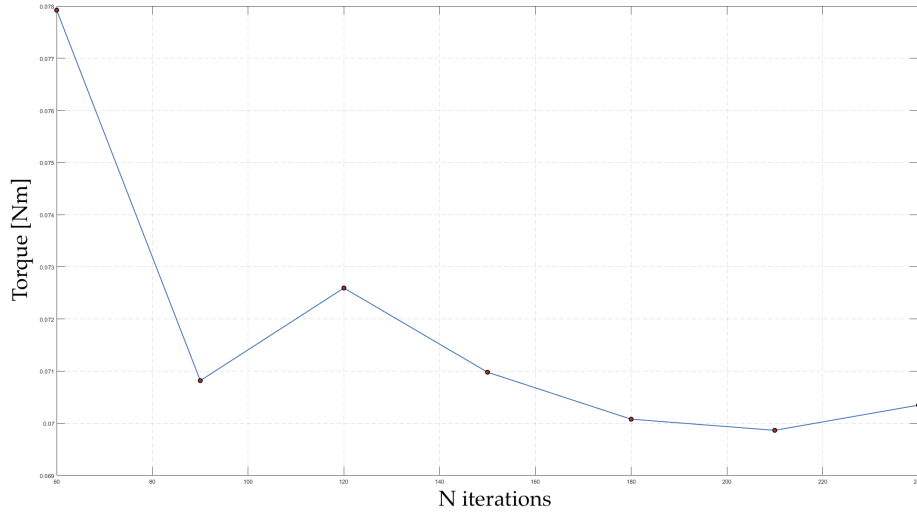
Figure 6.6: Average torque at different timestep values

required for these simulations varies significantly. Specifically, the simulation with the smaller timestep (0.5° per iteration) took approximately 103 minutes, whereas the simulation with the 0.8° timestep required 35 minutes less. This highlights the tradeoff between computational cost and solution accuracy.

Based on these results, a timestep of 450 iterations per revolution was selected for the final simulations. This corresponds to an angular step of 0.8°, which ensures sufficient resolution of the flow field across a wide range of wind speeds and rotational speeds while maintaining a manageable computational time.

6.3   Results

6.3.1   2D k-ω turbulence model

In this section, the results of over 40 simulations are presented. As discussed in the previous chapters, four different wind speeds (U_∞) are considered. For each wind speed, eleven simulations were conducted to accurately capture the power coefficient (C_p) curve. The choice of multiple points across the full operational regime is essential to ensure that the curve is represented with high precision.

It is important to note that the curves are not plotted strictly within the same λ (tip speed ratio) range as the experimental data. Instead, the simulation results cover a broader λ spectrum. This approach allows the full operational behavior of the turbine to be visualized, including regions beyond those explored

experimentally. By extending the λ range, the analysis offers a more comprehensive view of the turbine's performance across different conditions, ensuring a more complete understanding of its aerodynamic efficiency.
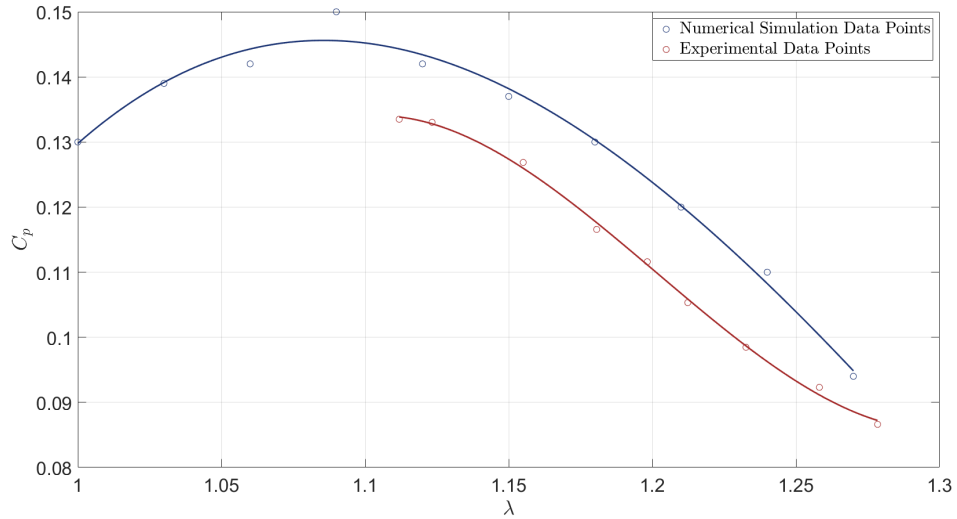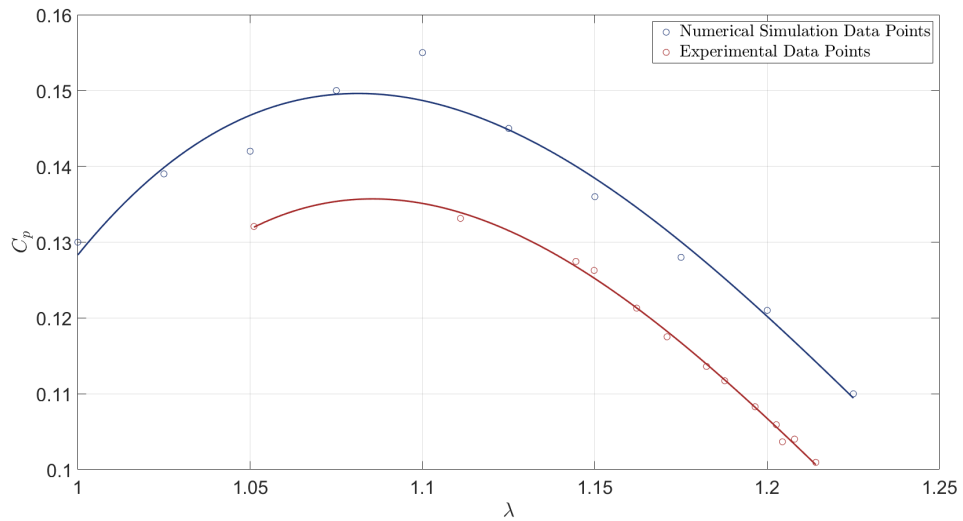

Figure 6.7: C_p-λ at $7\,m/s$ wind speed

Figure 6.8: C_p-λ at $8\,m/s$ wind speed

56
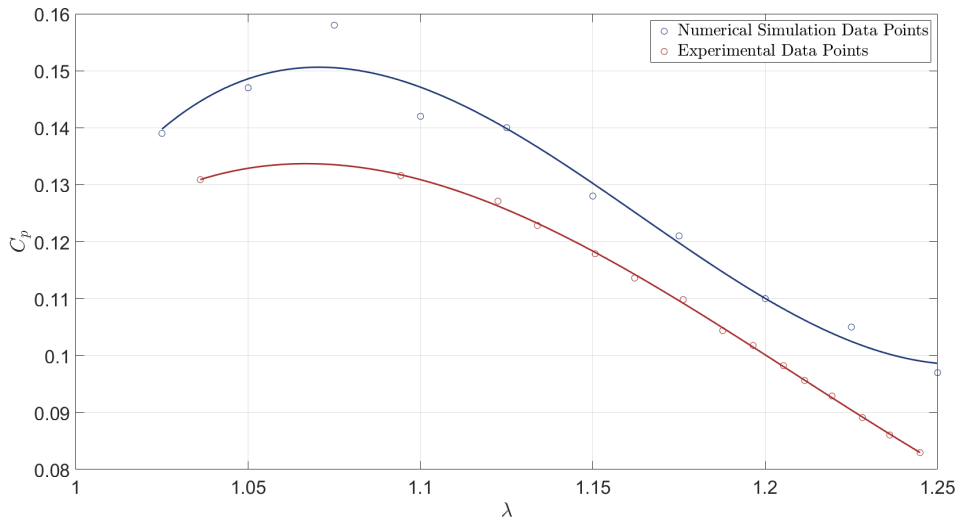
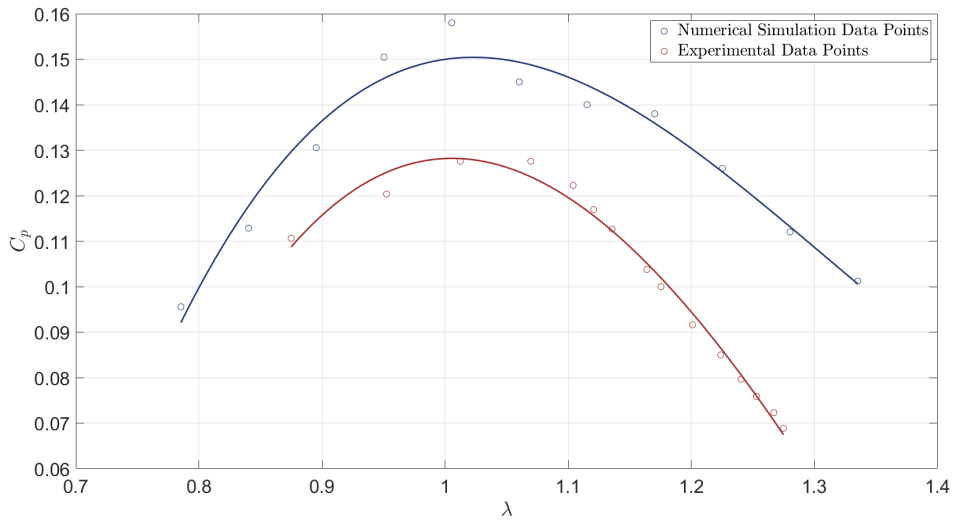**Figure 6.9:** C_p-λ at $9\,m/s$ wind speed

Figure 6.10: C_p-λ at $10\,m/s$ wind speed

As can be seen, a second-degree polynomial fit was applied to represent the general trend of the curves and enhance the readability of the graphs. This approach smooths out fluctuations in the raw data, providing a clearer visualization of the overall behavior. As indicated in the legend, the red line corresponds to the

57

experimental data from the case study, while the blue line represents the results obtained from the 2D simulations performed with the settings described in Chapters 5 and 6.

By applying the polynomial fit, it becomes easier to compare the experimental results with the simulation data, as the key trends and discrepancies between the two are more apparent. This method also allows for a better evaluation of the consistency and accuracy of the numerical model, highlighting areas where the simulation closely matches the experimental data and where deviations may occur.

Given the similarity of the four graphs, a general overview will be provided, with a specific focus on the curve obtained for the wind speed of 10 m/s. Overall, the first noticeable feature is the highly comparable trend between the experimental campaign and the data obtained from the fluid dynamics simulations. The peaks of the curves occur at very similar values of TSR.

The only exception is in the graph corresponding to a wind speed of 7 m/s. In this case, the lack of experimental data for lower TSR values makes it difficult to determine with absolute certainty whether the maximum value of the curve is captured within the displayed range. Nonetheless, the maximum possible error is estimated to be around 10%, which is still acceptable given that the simulations are two-dimensional, whereas the experimental data are inherently three-dimensional. This difference becomes even more significant when considering the highly turbulent nature of the flow, as turbulence is a fundamentally three-dimensional phenomenon.

For the same reason, the results obtained from the simulations tend to slightly overestimate the C_p values by just over 20% in some areas. This phenomenon is unavoidable and represents one of the primary disadvantages of conducting 2D simulations to describe a 3D phenomenon. However, as explained in the previous chapters, the advantages of running a preliminary study in 2D are numerous, and this approach is crucial for accelerating the overall process. Despite the limitations, the comparison remains useful and insightful, particularly when the inherent differences between 2D and 3D models are accounted for.

It is also important to note that the domain used during the simulation process does not perfectly replicate the experimental wind tunnel setup, which may contribute to the observed discrepancies in the results. This difference in domain configuration could explain certain deviations between the simulation and experimental data.

Focusing on the graph corresponding to the 10 m/s wind speed case, additional observations can be made. The simulations were carried out for a range of rotational speeds between 1000 and 1700 RPM, which is significantly broader compared to the other wind speed scenarios. This range covers TSR values from approximately 0.8 to over 1.3, providing a more comprehensive analysis of the turbine's performance.

One notable observation is the increasing divergence between the simulated

and experimental data at higher TSR values. This behavior can be attributed to the turbulent nature of the flow: as turbulence intensifies, the accuracy of two-dimensional simulations decreases, leading to larger discrepancies. Turbulence, being inherently three-dimensional, is challenging to capture accurately in 2D models, especially at higher flow regimes. Despite these limitations, the difference between the peak values of the curves remains within 5%, considering the TSR at which the maximum occurs. This is a highly satisfactory result, especially when factoring in the considerable reduction in computational time and resources achieved by utilizing two-dimensional simulations. The overall agreement between the simulations and experimental data demonstrates the effectiveness of the 2D approach for preliminary analysis, while also highlighting the areas where further refinements may be needed for higher accuracy.

6.3.2   2D k-ε turbulence model

Following the simulations conducted with the k-ω SST turbulence model, an additional study was performed to assess the accuracy of the Realizable k-ε turbulence model. This model has been frequently employed in numerous studies [18, 19, 20, 21], primarily due to its simplicity and ease of convergence, as discussed in Chapters 3 and 4. The Realizable k-ε model is advantageous for quick convergence and relatively straightforward implementation. No special modifications were required to implement this model, as the transition was straightforward within STAR-CCM+ by switching from the SST model to the Realizable k-ε model in the Physics section. All subsequent tests were conducted using the same setup and initial conditions employed throughout the thesis. Specifically, the wind speed (U_∞) and rotational speed (ω) were set at $10\,\mathrm{m/s}$ and $1000\,\mathrm{rpm}$, respectively.

The time history plot shown in Fig. 6.11 clearly highlights the primary weakness of the Realizable k-ε model, which is its inability to accurately model the near-wall subviscous layer in regions of the domain with steep adverse pressure gradients.

The cleaner and smoother shape of the Realizable k-ε curve reveals this deficiency. In an environment characterized by highly turbulent flow and complex vortex-airfoil interactions, the fluctuations in the averaged torque should be captured effectively, as is evident with the k-ω SST model.

Additionally, it can be observed that the peaks in the Realizable k-ε curve are significantly higher than those produced by the k-ω SST model, while the valleys, although negative, align closely with the blue curve. This results in a consistently higher average torque for the k-ε model, indicating a potential overestimation of the power output.

To further investigate the behavior of the Realizable k-ε model, a mesh convergence study was carried out using the same methodology outlined in Chapter 5. Similar to the k-ω SST model, the B3/B4 method was selected as it replicates the average
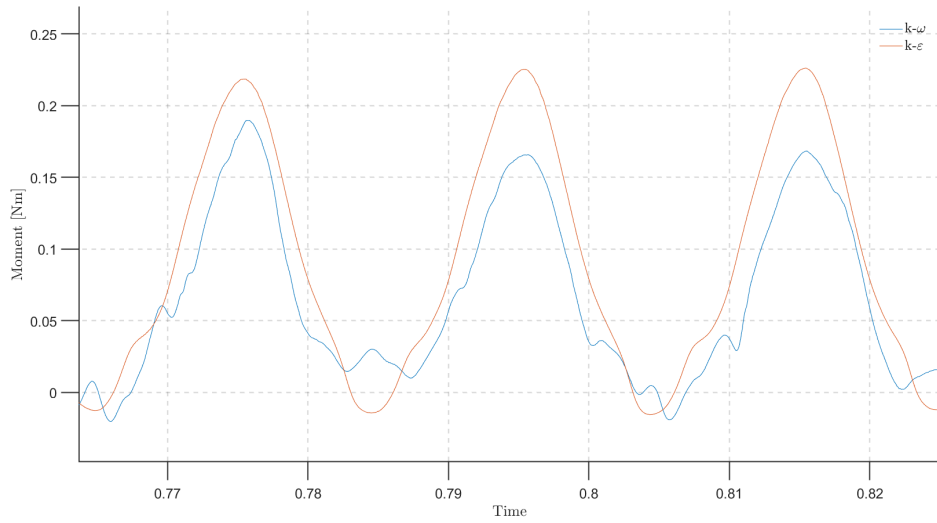
Figure 6.11: Time history comparison between k-ω SST and Realizable k-ε models

torque trend accurately, while the B2 method once again fails to provide reliable results.
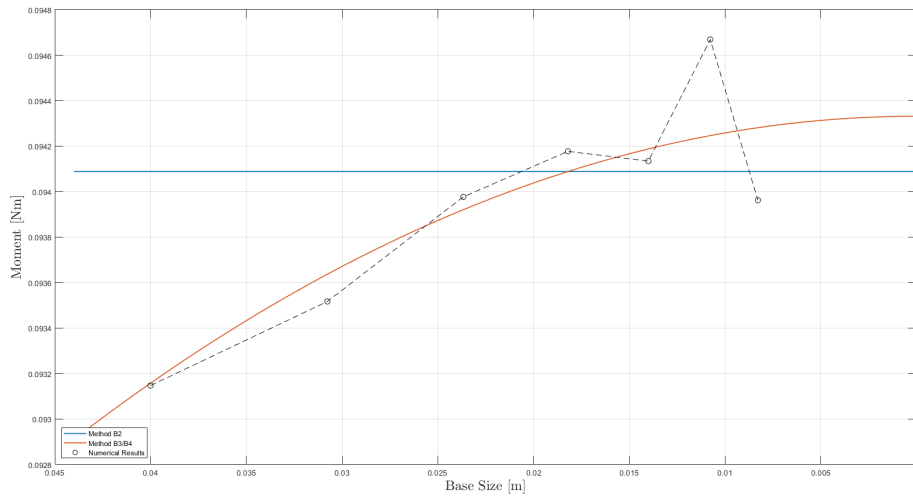

Figure 6.12: Realizable k-ε mesh convergence using Hoekstra's method

The convergence study reveals better accuracy for larger base sizes, though finer base sizes exhibit noticeable error. As previously explained in Chapter 6.1,

this could be attributed to insufficient time discretization, which may not be fine enough for this particular setup, leading to inaccuracies.
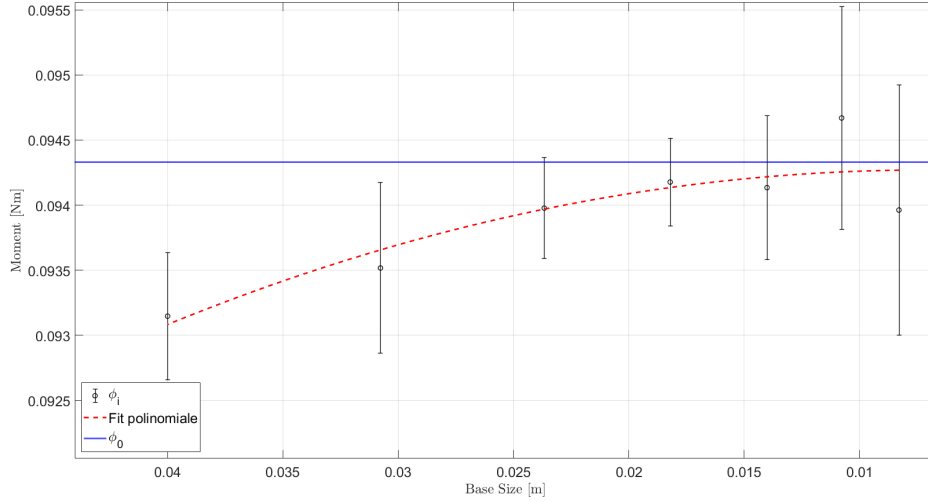

Figure 6.13: Realizable k-ε mesh convergence with errorbars and the polynomial fit displayed

One final point to note is the average torque value. For the chosen base size, the Realizable k-ε model yields a torque of $0.0942\,\mathrm{Nm}$, which is an 11% increase compared to the k-ω SST model. This discrepancy is consistent across other TSR values, indicating that the Realizable k-ε model tends to overestimate the power output.

The C_p-λ curve, shown in Fig. 6.14, further emphasizes the error introduced by the Realizable k-ε model. The green curve, representing the k-ε results, displays C_p values nearly three times greater than those obtained from experimental data. Although the overall trend of the curve remains similar, the magnitude of the C_p values renders the Realizable k-ε model unsuitable for generating accurate or even preliminary estimates.
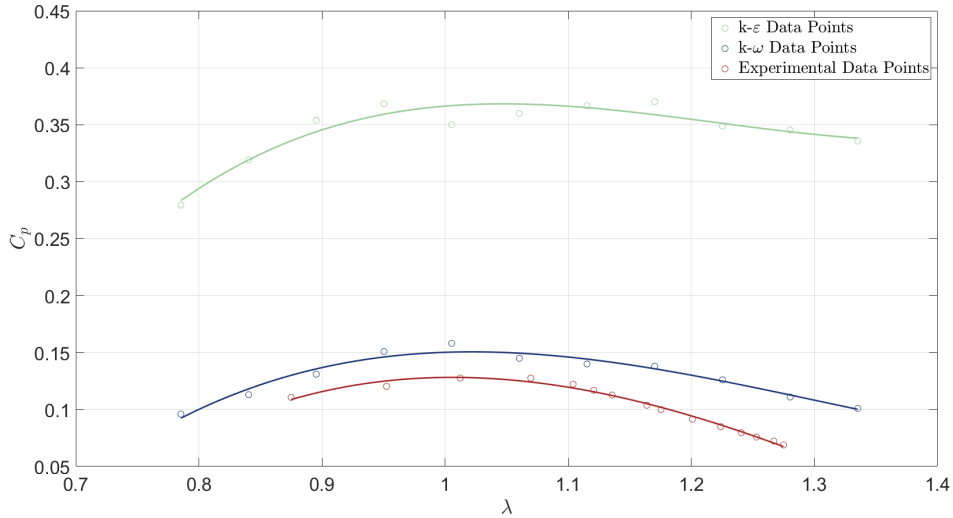
Figure 6.14: C_p-λ curve: the Realizable k-ε results are displayed in green

6.4 Validation with a 3D Simulation

To further confirm the accuracy and reliability of the model, a single 3D simulation was performed. This simulation, as with all initial tests conducted during this thesis work, was carried out at a wind speed of $10\,\mathrm{m/s}$ and a rotational speed of $1000\,\mathrm{rpm}$. As expected, the base size and timestep were kept consistent with the values studied earlier in the chapter, specifically $0.015\,\mathrm{m}$ and 450 iterations per revolution.

However, the mesh configuration and the dimensions of the computational domain differ from the 2D simulations. The fundamental mesh components remained consistent with those outlined in Chapter 5, with the key exception being the increased refinement applied to the wake region. To optimize the computational cost, the proportion of cells in different regions of the mesh was adjusted to reduce the overall cell count, resulting in a reduction from approximately 20×10^6 cells to 5.5×10^6. This is a common practice [28], since computational cost in unsteady simulations is still a huge challenge. As previously illustrated for the 2D simulations in Fig. 6.3, the relationship between simulation time and cell count is not linear, allowing the simulation time to be reduced by over 75%. Considering that over 40 hours of simulation time would have been required for the original mesh configuration, this adjustment resulted in a substantial reduction.

The adjustments focused mainly on reducing the cell density in certain regions, while maintaining sufficient accuracy. The main changes can be summarized as follows:
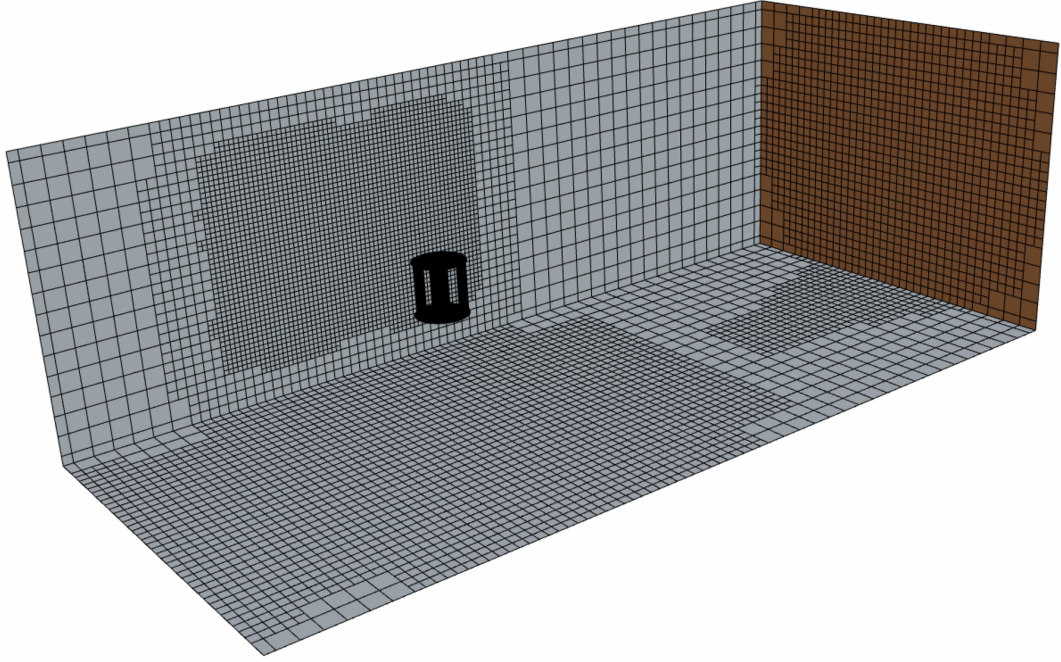
Figure 6.15: 3D domain of the simulation

- **Prism layer:** This is the densest region of the mesh and also the most computationally critical, as discussed in previous chapters. A balance between accuracy and discretization was achieved by reducing the number of prism layers to 20 and slightly increasing the target size in the surface control.

- **Areas adjacent to the blades:** These areas were also subject to increased cell size, taking care to avoid overly aggressive growth in cell size, which could negatively impact accuracy.

- **Overset zone:** The target size in this zone was increased to 50% of the base size, resulting in a significant reduction in the total number of cells within the computational domain.

These minor adjustments have significantly reduced the number of cells in the overset grid, bringing the total to approximately 3.8×10^6 cells. This value is consistent with similar studies conducted on comparable configurations [19, 38].

Regarding the entire computational domain, two key changes were made. First, the dimensions of the domain were adapted to match those of the computational domain used in the case study ($12D \times 8D \times 6D$). Second, the mesh type was switched from a polyhedral mesh to a trimmed mesh. This change helped improve both computational efficiency and mesh quality, particularly in regions of complex flow.
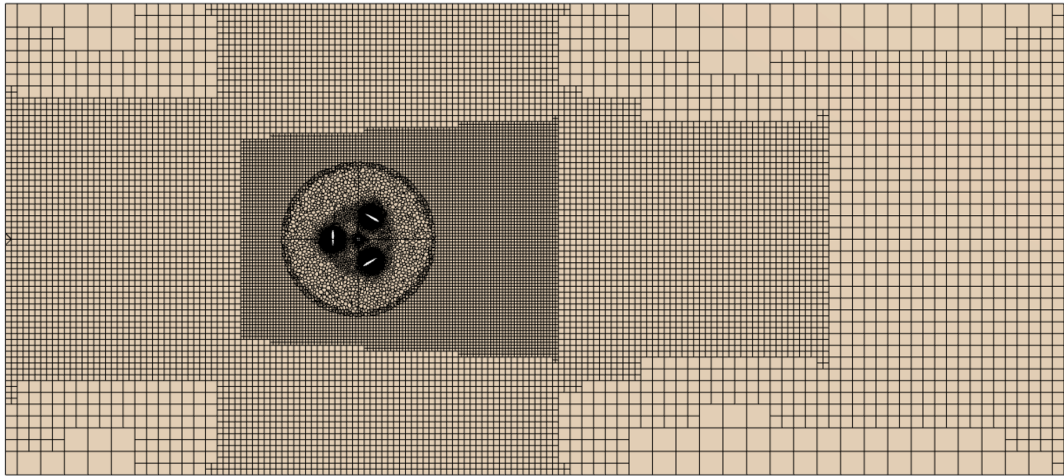
Figure 6.16: Section of the 3D mesh seen from above

These adjustments allowed for a significant reduction in computational time without sacrificing overall accuracy, making the 3D simulations more feasible while still providing reliable results. This balance of mesh refinement and computational efficiency was critical for ensuring that the 3D simulation could be completed within a reasonable timeframe.
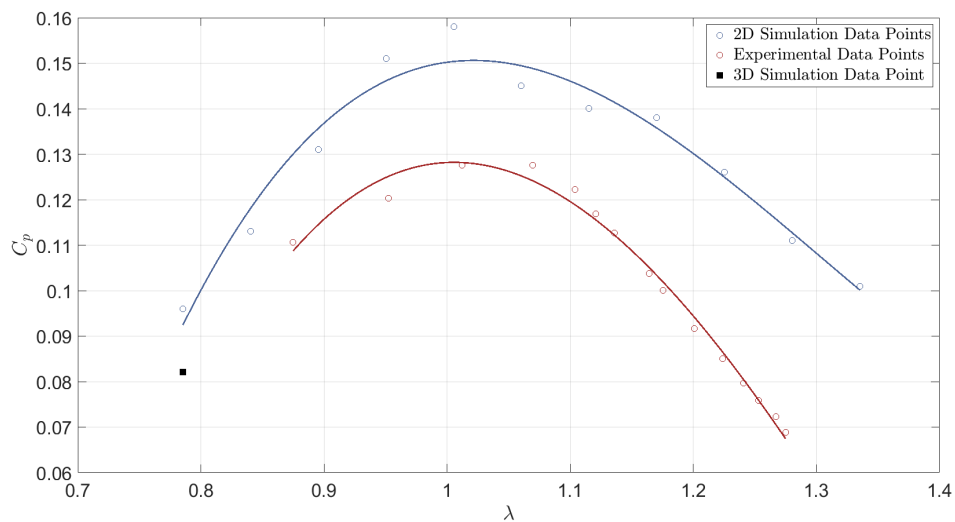

Figure 6.17: Comparison of results between 2D simulations (blue), experimental (red) and 3D simulation (black square)

As can be seen in Fig. 6.17, the C_p value for the same TSR of 0.7 is approximately 15% less in the 3D simulation. As mentioned before, this kind of result is to be expected [39] since the turbulence is a three-dimensional dissipative phenomenon, which cannot be fully captured by a two-dimensional simulation. While the TSR value falls outside the bounds of the available experimental data, it is reasonable to hypothesize that the simulation results remain consistent with the physical reality, particularly in a three-dimensional context. The discrepancy in the TSR range does not undermine the reliability of the model, as the overall behavior of the system is expected to be adequately captured, owing to the robustness of the 3D simulation framework. The coincidence between experimental and simulation data in such cases supports the accuracy of the model, but it is critical to acknowledge that validating the model across a broader range of conditions would require an extensive computational campaign. Simulating over 40 different cases would demand significant computational resources—both in terms of processing power and simulation time—that far exceed the practical limits of this thesis work. Instead of attempting such a vast replication effort, a single test case was selected to provide an initial assessment of the system's behavior under typical operating conditions. This approach offers a preliminary understanding of the model's predictive capabilities, even though a more comprehensive study would be needed to draw definitive conclusions about the entire parameter space. The focus on one simulation allows for a qualitative evaluation, ensuring that the key trends are captured without overwhelming computational resources.
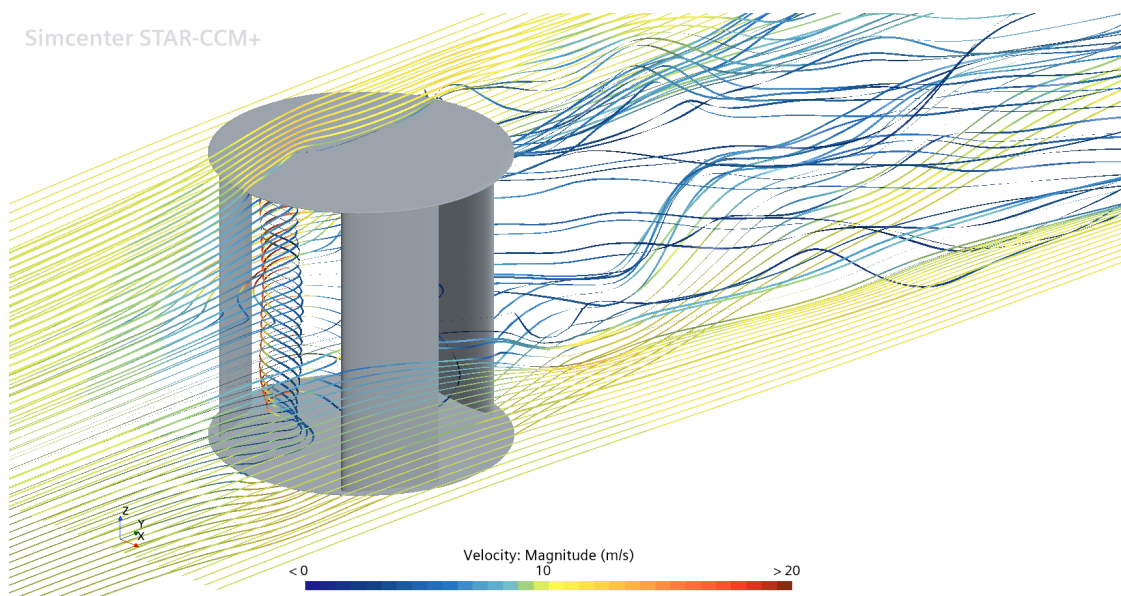

Figure 6.18: Velocity streamlines

Conclusion

In this thesis, various topics concerning the aerodynamics of Vertical Axis Wind Turbines (VAWT) were thoroughly investigated using advanced numerical techniques. A case study with available experimental data was selected with the objective of numerically replicating its conditions. To achieve this goal, several parameters were analyzed based on both a literature review and the experimental results of the study.

A comprehensive analysis of the k-ω SST turbulence model, developed by Menter, allowed for its precise implementation, which yielded highly predictive results. Subsequently, attention was directed towards the creation of a mesh that could satisfy the specific requirements of the flow field. This was followed by convergence studies and the selection of temporal discretization. All decisions were applied in a two-dimensional environment to reduce computational time during the setup phase.

The results of power coefficient (C_p) obtained were compared with those of the case study, while accounting for the differences between the 2D and 3D environments. A maximum error of approximately 20% was identified, which can be entirely attributed to the inability of 2D simulations to capture the dissipative phenomena caused by complex turbulent structures. Additionally, the realizable k-ε turbulence model was employed, but solely to illustrate its computational unreliability in regions with high negative pressure gradients.

A three-dimensional simulation was then conducted to validate both the numerical model and the experimental results. A 15% discrepancy was found between the 2D and 3D simulations, further confirming the accuracy and reliability of the model settings.

The aim of this work is to provide a solid starting point for future studies, consolidating the basic configurations of CFD simulations for VAWTs and equipping researchers with the necessary tools for accurate performance evaluation. The findings underscore the significance of considering three-dimensional effects when modeling VAWTs, while also presenting a structured approach for future computational research in this field.

Bibliography

[1] «Grover, R.D, and A.F Veneruso. Sandia Vertical-Axis Wind Turbine Program.» In: *Technical Quarterly Report, July–September 1976. [USA]. United States: N.p.* (1977).

[2] «Mohan Kumar, P.; Sivalingam, K.; Lim, T.-C.; Ramakrishna, S.; Wei, H. Review on the Evolution of Darrieus Vertical Axis Wind Turbine: Large Wind Turbines.» In: *Clean Technol. 1, 205-223.* (2019).

[3] «Paraschivoiu Wind turbine design: with emphasis on Darrieus concept.» In: *Polytechnic International.* (2002).

[4] «Didane, D.H.; Behery, M.R.; Al-Ghriybah, M.; Manshoor, B. Recent Progress in Design and Performance Analysis of Vertical-Axis Wind Turbines—A Comprehensive Review.» In: *Processes 2024, 12, 1094.* (2024).

[5] «Solomin, E., Lingjie, X., Jia, H., Danping, D. Comprehensive Comparison of the Most Effective Wind Turbines. In: Radionov, A., Karandaev, A. (eds) Advances in Automation. RusAutoCon.» In: *Lecture Notes in Electrical Engineering, vol 641. Springer, Cham* (2019).

[6] «West, J.R.; Lele, S.K. Wind Turbine Performance in Very Large Wind Farms: Betz Analysis Revisited.» In: *Energies 2020, 13, 1078.* ().

[7] «P. Deglaire, Stefan Engblom, O. Agren, and Hans Bernhoff. Analytical solutions for a single blade in vertical axis turbine motion in two-dimensions.» In: *European Journal of Mechanics - B/Fluids,28:506–520.* (2009).

[8] «P. G Migliore and W. P Wolfe. Effects of flow curvature on the aerodynamics of Darrieus wind turbines. United States.» In: (1980).

[9] «Anders Goude. Fluidmechanics of vertical axis turbines: Simulations and model development.» In: (2012).

[10] «Larsen J, Nielsen S, Krenk S Dynamic stall model for wind turbine airfoils.» In: *J Fluids Struct 23:959–982* (2007).

[11] «Ekaterinaris JA, Platzer MF Computational prediction of airfoil dynamic stall.» In: *Prog Aerosp Sci 33:759–846* (1998).

[12] «Wake modelling of a VAWT in dynamic stall: impact on the prediction of flow and induction fields Alessandro Zanon, Pietro Giannattasio and Carlos J. Simão Ferreira,» in: *WindEnerg. 18:1855–1874* (2015).

[13] «R Nobile, M Vahdati, J Barlow, A Mewburn-Crook. Dynamic stall for a vertical axis wind turbine in a two-dimensional study.» In: *World Renewable Energy Congress, Linköping, Sweden* (2011).

[14] «Dyachuk, E.; Goude, A. Simulating Dynamic Stall Effects for Vertical Axis Wind Turbines Applying a Double Multiple Streamtube Model.» In: *Energies, 8, 1353-1372* (2015).

[15] «Quan Wang, Boyang Liu, Cong Hu, Fengyun Wang, Shuyi Yang, Aerodynamic shape optimization of H-VAWT blade airfoils considering a wide range of angles of attack,» in: *International Journal of Low-Carbon Technologies, Volume 17, Pages 147–159* (2022).

[16] «Zhou, D., Zhou, D., Xu, Y. et al. Performance enhancement of straight-bladed vertical axis wind turbines via active flow control strategies: a review.» In: *Meccanica 57, 255–282* (2022).

[17] «Joshua Yen, Noor A. Ahmed, Enhancing vertical axis wind turbine by dynamic stall control using synthetic jets,» in: *Journal of Wind Engineering and Industrial Aerodynamics, Volume 114, , Pages 12-17,* (2013).

[18] «Marco Raciti Castelli, Alessandro Englaro, Ernesto Benini, The Darrieus wind turbine: Proposal for a new performance prediction model based on CFD.» In: *Energy, Volume 36, Issue 8, Pages 4919-4934* (2011).

[19] «Raciti Castelli, Marco, et al. Modeling strategy and numerical validation for a Darrieus vertical axis micro-wind turbine.» In: *ASME International Mechanical Engineering Congress and Exposition. Vol. 44441.* (2010).

[20] «F. Trivellato, M. Raciti Castelli, On the Courant–Friedrichs–Lewy criterion of rotating grids in 2D vertical-axis wind turbine analysis,» in: *Renewable Energy, Volume 62, Pages 53-62,* (2014).

[21] «M.H. Mohamed, Performance investigation of H-rotor Darrieus turbine with new airfoil shapes,» in: *Energy, Volume 47, Issue 1, Pages 522-530.* (2012).

[22] «A. Untaroiu, H.G. Wood, P.E. Allaire, R.J. Ribando, Investigation of Self-Starting Capability of Vertical Axis Wind Turbines Using a Computational Fluid Dynamics Approach, .» In: *J. Sol. Energy Eng. 133 4* (2011).

[23] «Robert Howell, Ning Qin, Jonathan Edwards, Naveed Durrani, Wind tunnel and numerical study of a small vertical axis wind turbine, .» In: *Renewable Energy, Volume 35, Issue 2, Pages 412-422* (2010).

[24] «Habtamu Beri and Yingxue Yao. Effect of Camber Airfoil on Self Starting of Vertical Axis Wind Turbine. .» In: *Journal of Environmental Science and Technology, 4: 302-312.* (2011).

[25] «Bo Yang, Chris Lawn, Fluid dynamic performance of a vertical axis turbine for tidal currents.» In: *Renewable Energy, Volume 36, Issue 12, Pages 3355-3366* (2012).

[26] «S. Lain, C. Osorio, Simulation and evaluation of a straight-bladed Darrieus-type cross flow marine turbine,» in: *J. Sci. Ind. Res. 69 (2010) 906e912.* (2010).

[27] «T. Maître, E. Amet, C. Pellone, Modeling of the flow in a Darrieus water turbine: Wall grid refinement analysis and comparison with experiments,» in: *Renewable Energy, Volume 51, Pages 497-512,* (2013).

[28] «A. Rossetti, G. Pavesi, Comparison of different numerical approaches to the study of the H-Darrieus turbines start-up,» in: *Renewable Energy, Volume 50, Pages 7-19,* (2013).

[29] «Simulating dynamic stall in a two-dimensional vertical-axis wind turbine: verification and validation with particle image velocimetry data C. J. Simão Ferreira, A. van Zuijlen, H. Bijl, G. van Bussel, G. van Kuik». In: *Wind Energy, volume 13, issue 1* (2010).

[30] «Menter, F. R. Improved Two-Equation Eddy-Viscosity Turbulence Models for Engineering Applications.» In: *AIAA Journal, 32(8), 1598-1605* (1994).

[31] «Wind Tunnel and OpenFOAM Flow Analysis of a High Solidity Vertical-Axis Wind Turbine Ahmed G. Yosry, Eduardo Á. Álvarez, Rodolfo E. Valdés, Joaquin F. Francos, Eduardo B. Marigorta». In: *Turbomachinery Technical Conference and Exposition GT2023* (2023).

[32] «Sengupta, A.R., Biswas, A. and Gupta, R. Studies of some high solidity symmetrical and unsymmetrical blade H-Darrieus rotors with respect to starting characteristics, dynamic performances and flow physics in low wind streams.» In: *Renewable EnergyVol.93 : pp.536–547.* (2016).

[33] «Roh, Sung-Cheoul and Kang, Seung-Hee. "Effects of a blade profile, the Reynolds number, and the solidity on the performance of a straight bladed vertical axis wind turbine."» In: *Journal of Mechanical Science and Technology Vol. 27 No.11: pp. 3299–3307.* (2013).

[34] «Subramanian, Abhishek, Yogesh, S Arun, Sivanandan, Hrishikesh, Giri, Abhijit, Vasudevan, Madhavan, Mugund- han, Vivek and Velamati, Ratna Kishore. "Effect of airfoil and solidity on performance of small scale vertical axis wind turbine using three dimensional CFD model. Energy Vol. 133(2017): pp.179–190.» In: *Energy Vol. 133: pp.179–190.* (2017).

69

[35] «Critical issues in the CFD simulation of Darrieus wind turbines Francesco Balduzzi, Alessandro Bianchini, Riccardo Maleci, Giovanni Ferrara, Lorenzo Ferrari». In: *Renewable Energy 85 419-435* (2016).

[36] «Critical issues in the CFD simulation of Darrieus wind turbines Francesco Balduzzi, Alessandro Bianchini, Riccardo Maleci, Giovanni Ferrara, Lorenzo Ferrari». In: *Renewable Energy 85 419-435* (2016).

[37] «Eça, L, and M Hoekstra. "A Procedure for the Estimation of the Numerical Uncertainty of CFD Calculations Based on Grid Refinement Studies.» In: *Journal of computational physics 262: 104–130* (2014).

[38] «C.J. Simao Ferreira, H. Bijl, G. van Bussel, G. van Kuik, Simulating dynamic stall in a two-dimensional vertical-axis wind turbine: verfication and validation with particle image velocimetry data .» In: *Wind Energy 13 (1) 1-17* (2010).

[39] «Acosta-López, J.G.; Blasetti, A.P.; Lopez-Zamora, S.; de Lasa, H. CFD Modeling of an H-Type Darrieus VAWT under High Winds: The Vorticity Index and the Imminent Vortex Separation Condition. Processes 2023». In: *Processes* (2023).

Questo lavoro di tesi mette la parola fine ad un percorso. Un percorso fatto di gioie, di momenti difficili, ma soprattutto di persone che hanno reso questa esperienza assolutamente indimenticabile.

Un ringraziamento speciale va a quelle anime pie che hanno dovuto sopportare le mie quotidiane lamentele.

Grazie mamma e grazie papà, che avete creduto in me in ogni momento, mettendo sempre una parola buona per confortarmi e spronarmi. Mi avete sostenuto, ma soprattutto mi avete insegnato la perseveranza che ha fatto di me la persona che sono oggi.

Grazie Luca per la tua costante presenza e le birrette di incoraggiamento, hai reso più leggero e spensierato questo lungo periodo.

Grazie Vale, amore della mia vita, per aver condiviso ogni singolo momento con me, dal terrore degli esami alle meritate e spensierate vacanze. Spero di essere per te anche solo un millesimo di quello che tu sei per me.

Un enorme grazie va anche ai miei amici, che per me rappresentano l'aspetto più bello di tutto il percorso universitario.

Grazie Matti, per essere stato un amico ancor prima di essere un compagno. Abbiamo condiviso alcuni dei miei migliori ricordi e sono certo che continueremo così.

Grazie Cate, con la tua genuinità e spensieratezza hai dato una nota di colore a questa grigia università.

Grazie Dido, per aver condiviso con me momenti difficili sempre con il sorriso e una birretta in mano.

Grazie Mario, per l'interminabile lista di meme e risate tirati fuori in questi tre anni.

Grazie Roby, per l'intrattenimento ludico a lezione e il tuo enorme senso del dovere che ha spronato tutto il gruppo.

Non vi ringrazierò mai abbastanza per essere stati a mani basse l'aspetto migliore dell'università.